


Title	Modifying germanium nanowires for future devices: an in situ TEM study
Author(s)	Kelly, Róisín Ann
Publication date	2016
Original citation	Kelly, R. A. 2016. Modifying germanium nanowires for future devices: an in situ TEM study. PhD Thesis, University College Cork.
Type of publication	Doctoral thesis
Rights	© 2016, Róisín Ann Kelly. http://creativecommons.org/licenses/by-nc-nd/3.0/ 
Embargo information	Restricted to everyone for one year
Embargo lift date	2017-06-17T09:05:14Z
Item downloaded from	http://hdl.handle.net/10468/2752

Downloaded on 2017-02-12T10:54:33Z

Modifying germanium nanowires for future devices: an in situ TEM study

Róisín Ann Kelly, B.Sc. (Hons)

Department of Chemistry
University College Cork
Ireland



UCC

Coláiste na hOllscoile Corcaigh, Éire
University College Cork, Ireland

**Presented for the degree of Doctor of Philosophy to the
National University of Ireland**

Supervisor: Dr Nikolay Petkov

Co-supervisor: Prof. Justin D. Holmes

Head of Department: Prof. Martyn Pemble

Declaration

I, Róisín Ann Kelly, certify that this thesis is my own work and I have not obtained a degree in this University, or elsewhere, on the basis of this thesis.

Róisín Ann Kelly

Abstract

Germanium was of great interest in the 1950's when it was used for the first transistor device. However, due to the water soluble and unstable oxide it was surpassed by silicon. Today, as device dimensions are shrinking the silicon oxide is no longer suitable due to gate leakage and other low- κ dielectrics such as Al_2O_3 and HfO_2 are being used. Germanium (Ge) is a promising material to replace or integrate with silicon (Si) to continue the trend of Moore's law. Germanium has better intrinsic mobilities than silicon and is also silicon fab compatible so it would be an ideal material choice to integrate into silicon-based technologies. The progression towards nanoelectronics requires a lot of in depth studies. Dynamic TEM studies allow observations of reactions to allow a better understanding of mechanisms and how an external stimulus may affect a material/structure. This thesis details in situ TEM experiments to investigate some essential processes for germanium nanowire (NW) integration into nanoelectronic devices; i.e. doping and Ohmic contact formation.

Chapter 1 reviews recent advances in dynamic TEM studies on semiconductor (namely silicon and germanium) nanostructures. The areas included are nanowire/crystal growth, germanide/silicide formation, irradiation, electrical biasing, batteries and strain.

Chapter 2 details the study of ion irradiation and the damage incurred in germanium nanowires. An experimental set-up is described to allow for concurrent observation in the TEM of a nanowire following sequential ion implantation steps. Grown nanowires were deposited on a FIB labelled SiN membrane grid which facilitated

HRTEM imaging and facile navigation to a specific nanowire. Cross sections of irradiated nanowires were also performed to evaluate the damage across the nanowire diameter. Experiments were conducted at 30 kV and 5 kV ion energies to study the effect of beam energy on nanowires of varied diameters. The results on nanowires were also compared to the damage profile in bulk germanium with both 30 kV and 5 kV ion beam energies.

Chapter 3 extends the work from chapter 2 whereby nanowires are annealed post ion irradiation. In situ thermal annealing experiments were conducted to observe the recrystallization of the nanowires. A method to promote solid phase epitaxial growth is investigated by irradiating only small areas of a nanowire to maintain a seed from which the epitaxial growth can initiate. It was also found that strain in the nanowire greatly effects defect formation and random nucleation and growth. To obtain full recovery of the crystal structure of a nanowire, a stable support which reduces strain in the nanowire is essential as well as containing a seed from which solid phase epitaxial growth can initiate.

Chapter 4 details the study of nickel germanide formation in germanium nanostructures. Rows of EBL (electron beam lithography) defined Ni-capped germanium nanopillars were extracted in FIB cross sections and annealed in situ to observe the germanide formation.

Chapter 5 summarizes the key conclusions of each chapter and discusses an outlook on the future of germanium nanowire studies to facilitate their future incorporation into nanodevices.

Acknowledgements

I would like to thank my supervisor Dr Nikolay Petkov for giving me this great opportunity and introducing me to the fascinating world of electron microscopy. As was stated by a past PhD student, “He is a very talented scientist and future generations of students could do well to pay attention to 50% of his ideas (the 50% that stand a chance of working).” He has some outrageously fantastic ideas, just figuring out how to implement them was the biggest challenge. I would also like to thank my co-supervisor Prof Justin Holmes for his help and guidance. I thank Dr Richard Farrell for giving me the initial push and helping me settle when I started the PhD. He was a great inspiration and his enthusiasm and drive are attributes I admire greatly. I thank Subhajt, Olan and Colm for keeping me supplied with grown Ge NWs. Thank you Anushka for all your work and help with the EBL. I thank Michael and Pat who I must have driven demented in EMAF. To my fellow MCAG members both past and present and the rest of the guys in 115 and 343, I thank you for making the time that bit easier and more enjoyable. I would also like to thank my collaborators Dr Bartosz Liedke, Dr Matthias Posselt and Mr Stefan Baldauf of Helmholtz Zentrum Dresden Rossendorf, Institute of Ion Beam Physics and Materials Research in Dresden.

I sincerely thank my family for their amazing support throughout my whole time in college. I thank Cian for being such a huge help and keeping me sane. Finally, I thank my son, Colm, for his incredible patience and understanding. He has endured 8 years of college with me and I think he deserves an honorary doctorate for that alone.

*Dedicated to my little goose, Colm. His inspirational quotes (taken out of context)
helped keep me going.*

“Focus!”

“Hey, back to writing!”

Published Articles

Included in this thesis:

Kelly, R. A.; Holmes, J. D.; Petkov, N., Visualising discrete structural transformations in germanium nanowires during ion beam irradiation and subsequent annealing. *Nanoscale* **6**, 12890-12897, doi:10.1039/c4nr04513k (2014). **Chapter 2**

Kelly, R. A.; Liedke, B.; Baldauf, S.; Gangnaik, A.; Biswas, S.; Georgiev, Y. M.; Holmes, J. D.; Posselt, M.; Petkov, N., Epitaxial Post-Implant Recrystallization in Germanium Nanowires. *Crystal Growth & Design* **15**, 4581-4590, doi:10.1021/acs.cgd.5b00836 (2015). **Chapter 3**

Other contributions:

Hobbs, R. G.; Farrell, R. A.; Bolger, C. T.; **Kelly, R. A.**; Morris, M. A.; Petkov, N.; Holmes, J. D., Selective Sidewall Wetting of Polymer Blocks in Hydrogen Silsesquioxane Directed Self-Assembly of PS-b-PDMS. *ACS Applied Materials & Interfaces* **4**, 4637-4642, doi:10.1021/am301012p (2012).

O'Driscoll, B. M. D.; **Kelly, R. A.**; Shaw, M.; Mokarian-Tobari, P.; Lontos, G.; Ntetsikas, K.; Avgeropoulos, A.; Petkov, N.; Morris, M. A., Achieving structural control with thin polystyrene-b-polydimethylsiloxane block copolymer films: The complex relationship of interface chemistry, annealing methodology and process conditions. *European Polymer Journal*, doi:http://dx.doi.org/10.1016/j.eurpolymj.2013.07.022.

Cummins, C.; Gangnaik, A.; **Kelly, R. A.**; Borah, D.; O'Connell, J.; Petkov, N.; Georgiev, Y. M.; Holmes, J. D.; Morris, M. A., Aligned silicon nanofins via the directed self-assembly of PS-b-P4VP block copolymer and metal oxide enhanced pattern transfer. *Nanoscale* **7**, 6712-6721 (2015).

Cummins, C.; **Kelly, R. A.**; Gangnaik, A.; Georgiev, Y. M.; Petkov, N.; Holmes, J. D.; Morris, M. A., Solvent Vapor Annealing of Block Copolymers in Confined Topographies: Commensurability Considerations for Nanolithography. *Macromolecular rapid communications* **36**, 762-767 (2015).

Cummins, C. Gangnaik, A.; **Kelly, R. A.**; Hydes, A. J.; O'Connell, J.; Petkov, N.; Georgiev, Y. M.; Borah, D.; Holmes, J. D.; Morris, M. A., Parallel Arrays of Sub-10 nm Aligned Germanium Nanofins from an In Situ Metal Oxide Hardmask using Directed Self-Assembly of Block Copolymers. *Chemistry of Materials* **27**, 6091-6096, doi:10.1021/acs.chemmater.5b02608 (2015).

Common abbreviations and acronyms

c/a: crystalline-amorphous

EBID: Electron beam induced deposition

EBL: Electron beam lithography

FEG: Field emission gun

FIB: Focused ion beam

Ge: Germanium

GeOI: Germanium-on-insulator

HRTEM: High resolution transmission electron microscopy

HSQ: Hydrogen silsesquioxane

IBID: Ion beam induced deposition

IPA: isopropyl alcohol

LMIS: Liquid metal ion source

NP: nanoparticle

NW: nanowire

RNG: Random nucleation and growth

sccm: Square cubic centimetres per minute

SEM: Scanning electron microscope

Si: Silicon

SiN: Silicon nitride

SPEG or SPER: Solid phase epitaxial (re)growth

SRIM: Stopping and range of ions in matter

STEM: Scanning transmission electron microscope

TEM: Transmission electron microscope

Contents

Declaration	i
Abstract	iii
Acknowledgements	v
Published Articles	vii
Common abbreviations and acronyms	viii
Chapter 1. Introduction	1
1.1. Abstract	2
1.2. Motivation and Background	2
1.3. Nanowire/Crystal growth	4
1.4. Germanide/Silicide Formation	10
1.5. Irradiation	15
1.6. Electrical Biasing.....	17
1.7. Batteries.....	21
1.8. Strain	24
1.9. Conclusions	28
1.10. References	29
Chapter 2. Experimental Methods	36
2.1. Instrumentation.....	37
2.2. Nanowire Fabrication	37
2.2.1. Grown Nanowires	38
2.2.2. Lithography defined fabricated nanowires	38
2.3. Nanowire Irradiation via FIB	39
2.3.1. Concurrent imaging platform for grown nanowires	39
2.3.2. Irradiation of grown nanowires	40
2.3.3. Irradiation of EBL defined GeOI Nanowires	42
2.4. HRTEM of irradiated nanowires	45
2.4.1. HRTEM of irradiated grown nanowires	45
2.4.2. HRTEM of irradiated lithography defined GeOI nanowires	45
2.5. In situ annealing of irradiated nanowires	46
2.6. Iradina (ion range and damage in nanowires)	46
2.7. Nickel-capped germanium nanopillar fabrication	47

2.8. TEM characterisation of Ni-capped Ge nanopillars	50
2.8.1. HRTEM of Ni-capped Ge nanopillars	50
2.8.2. In situ annealing of Ni-capped Ge nanopillars	50
2.9 References	51
Chapter 3. Investigating crystal damage in germanium nanowires due to ion beam irradiation	53
3.1. Abstract	54
3.2. Introduction	54
3.3. Experimental Procedure	56
3.3.1 Instrumentation	56
3.3.2 Nanowires	56
3.3.3. Concurrent imaging platform	57
3.3.4. Iradina (ion range and damage in nanostructures).....	59
3.4. Results and Discussion	59
3.4.1. 30 kV single exposure irradiation.....	59
3.4.2. Concurrent stepwise 30 kV irradiation	64
3.4.3. 5 kV irradiation.....	70
3.5. Conclusions	74
3.6. References	75
Chapter 4. Epitaxial post-implant recrystallization in germanium nanowires	78
4.1. Abstract	79
4.2. Introduction	79
4.3. Experimental Procedure	83
4.3.1. Concurrent imaging platform and irradiation	83
4.3.2. Irradiated EBL defined GeOI Nanowires	83
4.3.3. In situ anneal.....	86
4.4. Results and Discussion	86
4.4.1. Recrystallization of nanowire with extensive amorphisation.....	86
4.4.2. Recrystallization of nanowire with partial amorphisation.....	89
4.5 Conclusions	102
4.6 References	103
4.7. Appendix	109
Chapter 5. Investigating the formation of nickel germanides in germanium nanostructures	113

5.1. Abstract	114
5.2. Introduction	114
5.3. Experimental.....	117
5.3.1. Ni-capped Ge nanopillar preparation.....	117
5.3.2. TEM Characterization.....	121
5.4 Results and Discussion	121
5.4.1 Sample 1	121
5.4.2. Sample 2	129
5.4.3. HRTEM of Ni seeded Ge NW growth	136
5.5. Conclusions	138
5.6. References	138
5.7 Appendix	142
Chapter 6. Conclusions and Outlook.....	143
References	148



Kelly, R.A 2016. Modifying germanium nanowires for future devices: an in situ TEM study. PhD Thesis, University College Cork.

Please note that Chapter 1 (pp.1-35) is unavailable due to a restriction requested by the author.

CORA Cork Open Research Archive <http://cora.ucc.ie>

Chapter 2

Experimental Methods

2.1. Instrumentation

An FEI Helios 600i NanoLab dual beam system (SEM/FIB) was used for all SEM imaging, ion irradiations and TEM lamellae sample preparation. The SEM is equipped with a FEG (field emission gun) source and the FIB with a Ga LMIS (liquid metal ion source). An omniprobe needle facilitates TEM lamella preparation.

A JEOL 2100, LaB₆ filament source, TEM was used for all TEM imaging. For HRTEM, a Gatan double tilt holder was used to allow tilt in two axes which facilitates tilting a crystal to a zone axis. For heating experiments, a Gatan 628 single tilt heating stage holder was used. The stage operates as a micro furnace and is capable of temperatures of 1000 °C but a maximum temperature of 500 °C was used in this thesis. Temperature was controlled using a Gatan Model 901 SmartSet hot stage controller. The temperature dispersion control is approximately 0.1–0.5 °C, as per the manufacturer's specifications.

A Raith eLine EBL system was used for all EBL exposures. The system is a converted SEM with a laser stage which allows for accurate movement of the stage for patterning.

2.2. Nanowire Fabrication

Two types of nanowires were used in this thesis; grown (bottom up) and GeOI lithography defined (top-down) nanowires.

Chapter 2. Experimental Methods

2.2.1. Grown Nanowires

The grown nanowires were supplied by Dr Subhajit Biswas, Dr Olan Lotty and Dr Colm O'Regan. A SCF (supercritical fluid) method of synthesis for the grown Ge NWs was used which occurs via a VLS-type (vapour-liquid-solid) mechanism.¹⁻⁴ The nanowires are grown on Si substrates with a dispersion of Au nanoparticles which act as the seed for growth. The grown nanowires appear like a forest of nanowires on the substrate. Typically, nanowires are removed from the substrate by sonication in isopropyl alcohol (IPA) to produce a suspension of nanowires. This introduces organic solvent contamination and which can be difficult to remove, leaving residue and diminishing the ability of HRTEM. To avoid this, a dry transfer method was used in this work. A scalpel was used to gently remove some NWs from the substrate and transfer to the sample platform, e.g. the SiN membrane.

2.2.2. Lithography defined fabricated nanowires

The lithography defined Ge NWs are fabricated from GeOI substrates using HSQ (hydrogen silsesquioxane) resist in a Raith eLine EBL system by Dr Anushka Gangnaik.⁵ All GeOI NWs were defined via EBL from a (001) GeOI wafer along the [100] direction. HSQ is a high resolution negative tone resist which when exposed to the electron beam, becomes insoluble to the developer solution, TMAH (tetramethylammonium hydroxide). As Ge reoxidises rapidly in ambient conditions, a citric acid clean was used to remove the oxide and passivate the surface prior to HSQ resist deposition.⁶ A 2.4% HSQ (in methyl isobutyl ketone) solution was deposited directly after the oxide removal step via spin coating at 2000rpm for 33s.⁵ The resist film was baked on a hotplate at 120 °C for 3 min, to remove any solvent from the resist. The EBL was operated at 10 kV and exposure doses were set

Chapter 2. Experimental Methods

depending on the NW diameter desired; $1000 \mu\text{Ccm}^{-2}$ for 1 μm diameter and $2300 \mu\text{Ccm}^{-2}$ for 20 nm diameter. Essentially, the HSQ forms a SiO_2 mask which can be used as a hard mask for etching. After EBL exposure, the sample was immersed, with agitation, in 2.3% TMAH at room temperature for 70 s, followed by a 30 s rinse in deionised water and then dried in flowing nitrogen for 10 s. The exposed Ge was etched, as described by Ran et al., in a Cl_2 RIE at 80W, 10mTorr, with a flow rate of 30 sccm, for 25 s.⁷

2.3. Nanowire Irradiation via FIB

2.3.1. Concurrent imaging platform for grown nanowires

Grown NWs were transferred to a modified SiN membrane carrier chip platform for concurrent TEM imaging and FIB irradiation. The carrier chip platform used for step-wise implantation/imaging of a specific nanowire is shown in Figure 2.1. Si chips with silicon nitride (SiN) membrane windows were used (Ted Pella), which were patterned using the FIB to label and open slits in the membrane. The patterning is of benefit for two reasons; the slits allow high resolution imaging of sections of the nanowire as well as facile navigation to locate the same nanowire. The parameters for patterning were: 7 lines $10 \mu\text{m}$ apart, $70 \mu\text{m}$ long and $0.5 \mu\text{m}$ wide for a nominal depth of 300 nm with the Ga ion beam operating at 30 kV, 3 nA.

Chapter 2. Experimental Methods

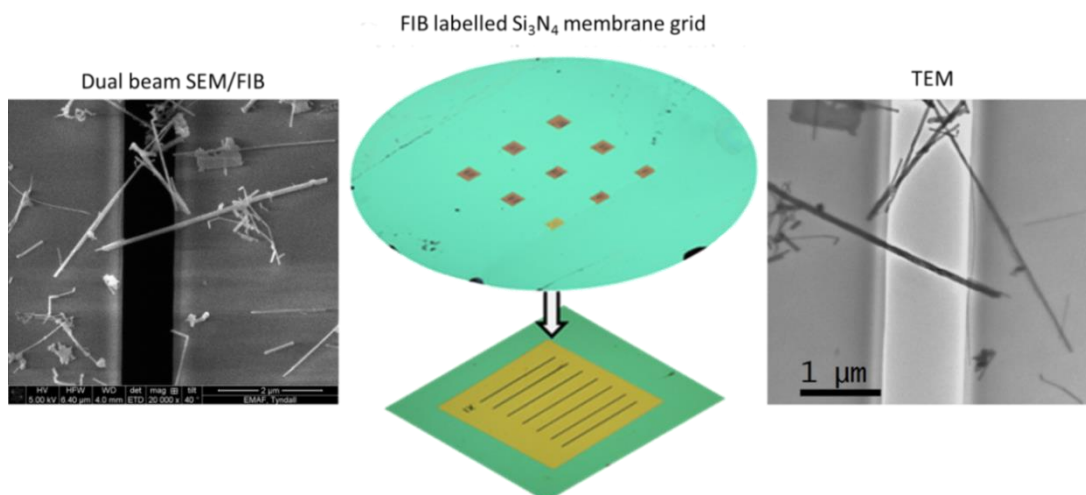


Figure 2.1. Overview of platform for correlative imaging of nanowire on Si_3N_4 membrane grid.

2.3.2. Irradiation of grown nanowires

The grown NWs were first imaged in the TEM where the growth direction, tilt to achieve a low index zone axis and any intrinsic defects were identified. Nanowires that required no more than 10 degrees tilting in one direction, preferably along or perpendicular to their long axis, and fully crossed the opening were selected. The mounting of the membrane chips to the TEM holder was done with the aid of an optical microscope, ensuring the grid is mounted with a fixed orientation. This allows the nanowires to be imaged in the same orientation after each exposure. This accurate mounting method becomes more important as the nanowire reaches a near/fully amorphous state. The grid was then transferred to the SEM/FIB for implantation. All NW irradiation was done using an FEI Helios 600i NanoLab Dual Beam system. The nanowire was located using the SEM and then orientated (stage was rotated and moved in x- and y-directions) so that the nanowire length was at eucentric height when the stage was tilted, i.e. the nanowire was aligned left to right in the SEM. The stage was tilted to 52° so the FIB is normal to the substrate surface.

Chapter 2. Experimental Methods

The position of the NW was saved. The arrow keys, left or right to keep the changing only the y-coordinate, were used to navigate to the edge of the sample. This is to find a safe area away from the NW to align the SEM with the FIB. A feature was identified, without changing the x-coordinate, in the SEM and using beam shift for the ion beam (at 30 kV, 9.7 pA or 5 kV, 10 pA) the same feature was centred. Moving stepwise (one or two clicks of the left/right arrow) back to the NW to be irradiated the alignment was adjusted/checked at increasing magnification to ensure the alignment between SEM and FIB was accurate. Once the NW was within view in the SEM, imaging with the FIB was stopped. Any imaging with the FIB would introduce Ga⁺ ions at an unknown dose. With the SEM only, the NW was centred. Assuming accurate alignment with the FIB, the NW should be in the centre of the FIB screen also. The irradiation needs to be done “blind”.

Most exposures were done at this tilt unless the tilt required for a nanowire in the TEM is <2°, in this case the stage was tilted to 45° to avoid ion channelling. The pattern for implantation was defined in the ion beam window as a rectangle set to Si mill application: 10 × 10 μm² area, 125 ns dwell time, 1 pass and with a total time of 0.316 s to achieve a dose of 1.9 × 10¹³ ions cm⁻², operating at 30 kV (or 5 kV), 9.7pA (10pA aperture at 5kV). For partial irradiation of a NW along its length, a 0.5 × 5 μm² box was defined, to irradiate a 0.5 μm length section of the NW. The dose was calculated using

$$dose = \frac{I_{ion} \times t_{exposure}}{A_{pattern} \times 1.602 \times 10^{-15}}$$

Chapter 2. Experimental Methods

where I_{ion} is the current/aperture used in pA (9.7 or 10 pA), $t_{exposure}$ is the time of the exposure in seconds (0.316 s) and $A_{pattern}$ is the area of the pattern ($100 \mu\text{m}^2$). Higher doses were achieved by increasing the number of passes.

The carrier chip was then transferred back to the TEM in the same orientation to image the nanowire after doping. The concurrent implantation/imaging steps were repeated multiple times to build up the step-wise increase in the dose. The maximum implantation dose in our studies was 1.14×10^{14} ions cm^{-2} which corresponds to 6 successive steps. Once the exposure of NWs deposited on SiN membrane grids with trenches was completed, the sample could be directly transferred to the TEM for imaging and even undergo further irradiation.

2.3.3. Irradiation of EBL defined GeOI Nanowires

The method of Ga^+ ion irradiation for grown and lithography defined NWs is nearly identical to grown nanowires, the main difference is how we observe the irradiation damage post anneal and the limitation of only one irradiation event. An overview of the experimental procedure for the irradiation and imaging of NWs is depicted in a schematic in Figure 2.2. NWs deposited on silicon nitride (SiN) membranes do not require any additional steps for observing the damage incurred and subsequent in situ TEM annealing (Figure 2.2 a).⁸ The method described in this section is used for grown NWs deposited on a Si/SiO₂ chip via dry transfer from the growth substrate or EBL defined NWs on GeOI (germanium on insulator). In order to observe irradiation damage and in situ TEM recrystallization along the NWs on substrates, the structures need to be extracted with the underlying substrate (Figure 2.2 b iii). This is done via a non-typical inline FIB lift-out technique along the NW length (Figure 2.2 b, Figure 2.3). For all NWs imaged on SiN membranes, the direction of the ion beam (red

Chapter 2. Experimental Methods

arrow) during irradiation is nearly parallel to the electron beam (purple arrow) when imaged in the TEM (Figure 2.2 a). However, for NWs extracted from a substrate (Figure 2.2 b) the direction of the ion beam is orthogonal to the direction of the electron beam when imaged in the TEM, i.e. we have a side view of the irradiated NW along its length.

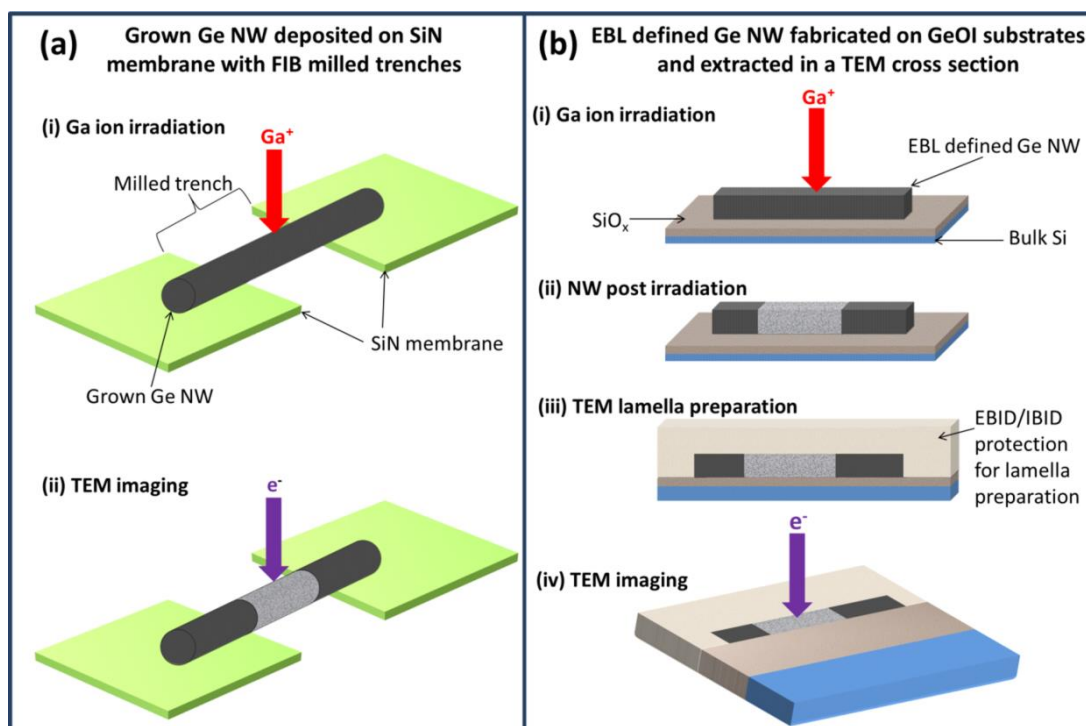


Figure 2.2. Schematic overview of sample preparation and imaging for (a) a nanowire on pre-patterned SiN membrane and (b) EBL defined NW from on GeOI substrate.

The GeOI NWs defined by EBL have a height of approximately 50 nm, which is almost twice the range of interactions of the 30 kV Ga-ions in Ge. Therefore, to achieve amorphisation across the NW (the width of the NWs is approximately 40 nm) and avoid ion channelling, very high ion-beam incidence angles ($\pm 62^\circ$) were used (Figure 2.4), achieved by tilting the stage to -10° , adding to the 52° tilt of the FIB column.

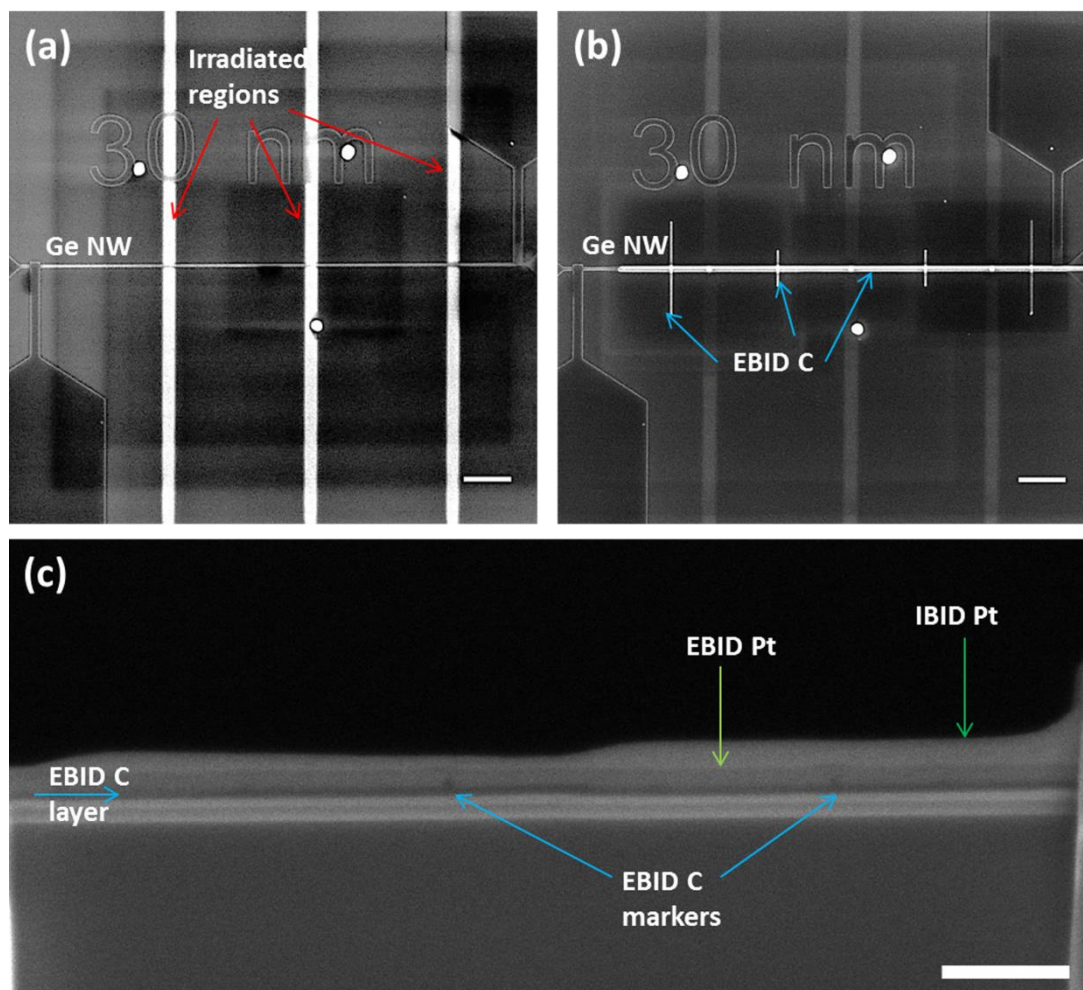


Figure 2.3. Overview of use of EBID carbon for indication of NW exposure during thinning. Scale bar for all images is 1 μm .

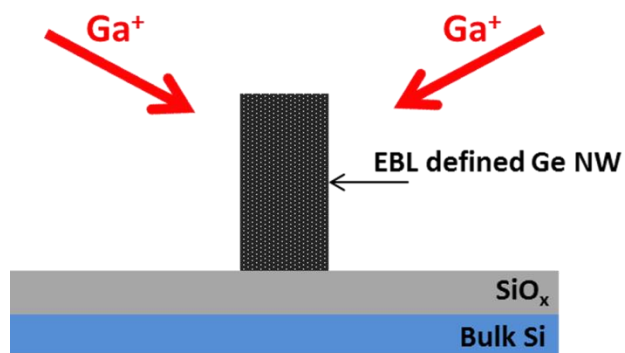


Figure 2.4. Schematic of 62° tilt ion irradiation of EBL defined Ge NW in cross sectional view.

2.4. HRTEM of irradiated nanowires

The Gatan double tilt holder was used for high resolution TEM (HRTEM) imaging as tilt in two directions is nearly always required to orient a NW to a zone axis. To tilt to a zone axis, the convergent beam electron diffraction (CBED) pattern was used to navigate the orientation until a symmetric pattern was achieved. Once a zone axis was achieved, a selected area diffraction (SAD) pattern was acquired by inserting the selected area aperture and spreading the beam. To protect the CCD camera, the beam blank was inserted to block the direct beam.

2.4.1. HRTEM of irradiated grown nanowires

NWs were transferred to labeled/trenched SiN membranes via dry transfer. There were nine $200 \times 200 \mu\text{m}^2$ membrane sites per grid, each was labelled (for identification) and patterned (to open trenches for HRTEM) with the FIB. NWs which lay securely across a trench and required no more than 10 degrees tilting to a low index zone axis for lattice resolution imaging were selected for irradiation. The tilt required for a specific zone axis was recorded as well as any intrinsic defects. Images of the position of the NW as well as lattice resolution images were acquired.

2.4.2. HRTEM of irradiated lithography defined GeOI nanowires

Irradiated GeOI NWs were extracted in TEM lamellae, as described in section 2.3 Irradiation of EBL defined GeOI Nanowires. The GeOI is fabricated such that the Ge layer crystal is in the same orientation as the bulk Si carrier. This makes the tilt to zone axis easier as the bulk Si can be used for this. All of the GeOI NWs are defined with a “growth direction” in [100] direction and hence the zone axis imaged is [010].

2.5. In situ annealing of irradiated nanowires

An in situ Gatan Model 628 single-tilt heating stage TEM holder was used for all anneals presented in this study. The ramp/temperature used for each NW varied. The sample was loaded in the same orientation in the in situ heating stage as it was for HRTEM imaging in the double tilt holder. The in situ heating stage is only capable of single tilt so the sample was tilted as close to the zone axis used for high resolution imaging as possible. For most samples tilting in two directions is required to achieve a zone axis orientation for lattice resolution imaging. The TEM was operated in bright field mode, isolating the direct beam with the objective aperture, to take advantage of the contrast between the crystalline and amorphous regions. Temperature was controlled using a Gatan Model 901 SmartSet hot stage controller. Temperatures varied from 100 – 500 °C (the temperature dispersion control is approximately 0.1 - 0.5 °C, as per the manufacturer's specifications). Images were acquired every minute at the set temperatures.

2.6 Iradina (ion range and damage in nanowires)

Iradina was used to simulate ion beam irradiation in Ge nanowires. The material of the wire was defined as Ge and the surrounding material set as vacuum. For this experimental procedure the nanowire was defined as a cylinder with a varied diameter, 65 nm, 45 nm or 25nm. The accelerating voltage was set to 5 kV or 30 kV for the Ga ion source. A section of the nanowire was defined by the periodic boundary conditions (PBC), essentially defining a 2 dimensional cross section of the nanowire, which in turn is divided into a number of cells (defined by the user). For the results presented here, the PBC was set at $80 \times 80 \text{ nm}^2$, with the individual cells

Chapter 2. Experimental Methods

set at $0.5 \times 0.5 \text{ nm}^2$. The ion beam direction is set orthogonal to the nanowire length as the crystallinity of the material is disregarded due to random phase approximation (RPA) of the target atoms so any ion channeling in the crystal is not accounted for.

2.7 Nickel-capped germanium nanopillar fabrication

The process flow for the fabrication of Ni-capped Ge nanopillars is illustrated in Figure 2.5. A method to produce nanopillars of Ge with varied diameters has been developed with the use of EBL. Ni-capped germanium nanopillars were fabricated on Ge(001) substrates. A positive tone EBL resist was used to expose desired circular areas on the Ge substrate as shown in Figure 2.5.

Initially, a two layer (PMMA-copolymer) EBL resist was used to facilitate a facile metal lift process. However, an undesirable lip of Ni was observed for the pillars, which is attributed to the collapse of the upper resist during metal evaporation. As the metal is used as a mask for etching, this results in larger diameter pillars than desired. Hence, for further sample preparation the Ge substrate was patterned by EBL using SML-50, a high resolution positive tone EBL resist.⁹ Single pixel dot exposures, with $1 \mu\text{m}$ pitch, were defined in a line with large markers on either side.

The diameters of the dots were varied with the dose (dwell time) at each spot; the diameter increases with increasing dose. The dose range used was $0.2 - 6.4 \text{ fC}$ per single exposure and the electron beam was operated at 10kV accelerating voltage. After exposure, the resist was developed in 7:3 IPA/deionised water for 30 s followed by IPA for 15 s and dried under a flow N_2 for 30 sec. A 50 nm thick Ni layer was evaporated, by electron beam evaporation, onto the patterned substrate

Chapter 2. Experimental Methods

followed by a metal lift-off in acetone to achieve Ni dots (and markers) on the Ge substrate. The Ge was etched, using the Ni as the hard mask, in a Cl reactive ion etch (RIE) at 20 °C, 30 sccm Cl₂, 10 mtorr and 80W RF.⁷

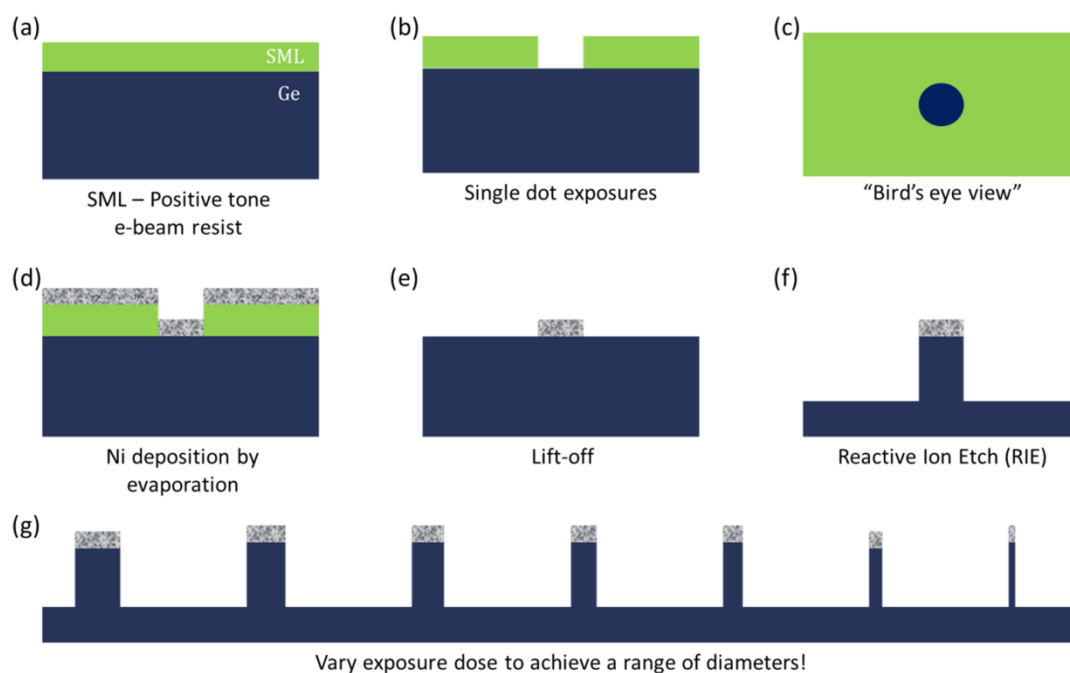


Figure 2.5. Process flows of Ni-capped Ge nanopillars using SML resist.

For annealing experiments, a line of pillars was extracted in a cross section and transferred to an omniprobe grid, as shown in Figure 2.6. To help aid in polishing the cross section to the region of interest, a line of EBID carbon was deposited along the line of dots with a total nominal height of 1 μm , similar to the method described for inline nanowire cross sections described previously in chapter 2. This helps to ensure cut placement and aids in the final FIB polishing of the cross section because the EBID-C has good contrast against the platinum (Pt) protection. The EBID-C also acts as an insulation layer to encapsulate the Ni/Ge pillars. The next layer of protection with the dimensions 15 μm \times 2 μm and a nominal height of 250 nm of EBID-Pt was deposited followed by 2 μm ion beam induced deposition (IBID) Pt.

Chapter 2. Experimental Methods

During thinning, the cross section was polished only from the front side, by turning the grid 180° with a stage rotation to polish the other side from the front for accurate final polishing.

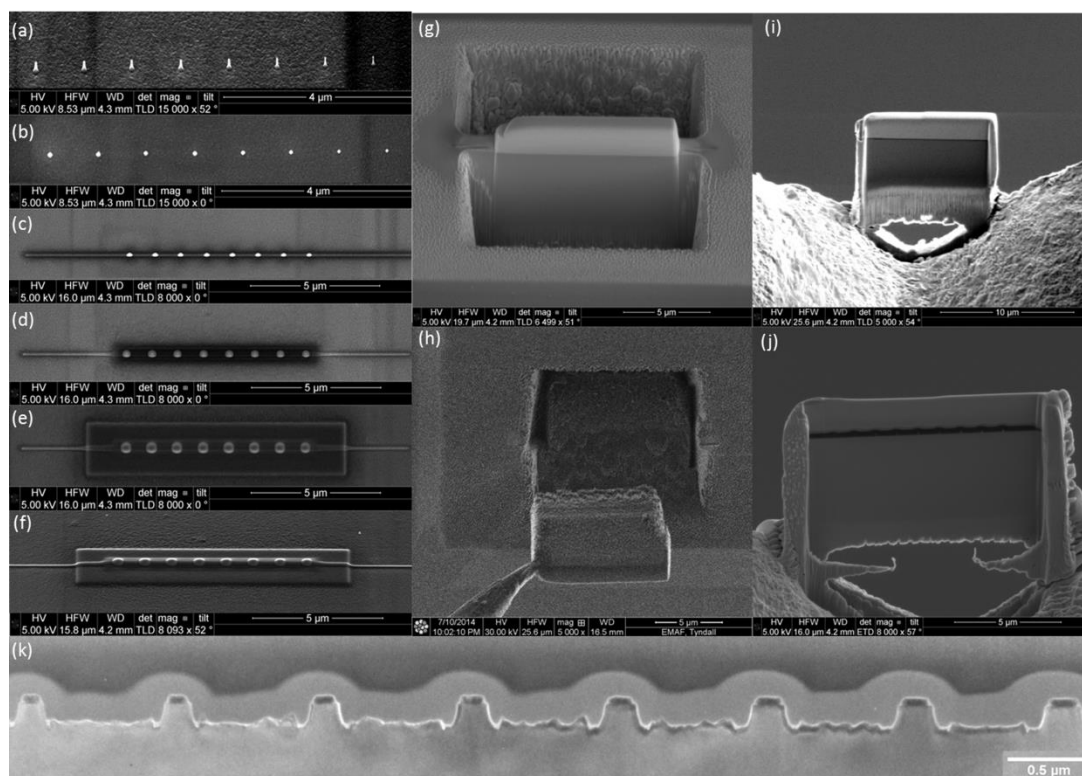


Figure 2.6. Overview of extraction of Ni-capped Ge nanopillars in a TEM lamella. (a) Tilted view of nanopillars. (b) "Birds eye view" of nanopillars. (c) EBID-C line deposited along nanopillars. (d) EBID-Pt as protection of ion beam. (e) Initial IBID-Pt for lamella preparation. (f) Tilted view of initial IBID protection showing nanopillars are fully encapsulated. (g) Trenches milled (with the FIB) either side of the lamella to be extracted. (h) Lamella extracted using omniprobe which transfers the lamella to the omniprobe grid. (i) Lamella attached to the omniprobe grid at the two base points for added stability during in situ annealing experiments. (j) Lamella during thinning process using FIB, dark line of C-protection observed as well as the bumps which show the topography of the nanopillars and hence the endpoint of thinning is close. (k) Example of TEM image of array of nanopillars of increasing diameters extracted in a TEM lamella.

A native GeO_x removal step is required before EBL resist deposition to optimise the surface to avoid dewetting and achieve a uniform resist. The water soluble oxide is removed in a 30 s dip in deionised water, followed by a re-oxidation of surface with a 30 s dip in 4.5 M nitric acid (HNO_3) and a final oxide removal and surface

Chapter 2. Experimental Methods

passivation step in 10% HCl for 10 min.¹⁰ No oxide removal step was performed on the exposed surface before metal evaporation, which could be a major factor for the rough Ge/Ni interface. Ideally, the sample should be placed directly in the metal evaporator post resist development to avoid oxidation of Ge in ambient air.^{11,12}

2.8. TEM characterisation of Ni-capped Ge nanopillars

2.8.1. HRTEM of Ni-capped Ge nanopillars

Before annealing, the structures were imaged using a Gatan double tilt imaging holder in a JEOL 2100 HRTEM and tilted to a low index zone axis for HTREM imaging. The bulk substrate was used to orientate the sample into a zone axis. HRTEM images were acquired of the interface between Ge and Ni interface. After the anneal, the bulk Ge is unchanged and hence can be used to find the same zone axis and orientate the nanopillars as they were for HRTEM before the anneal. Lattice resolution images were acquired of the Ge-Ni interface. Because of the size of the germanide region, acquiring a SAED pattern alone is difficult without contribution from the Ge crystal. Lattice resolution images were required to be able to obtain fast Fourier transforms (FFTs) from lattice resolution images to determine germanide phase and orientation.

2.8.2. In situ annealing of Ni-capped Ge nanopillars

A Gatan 628 single tilt heating holder was used for in situ annealing. The pillars were imaged in bright-field mode using the smallest objective aperture during the anneal to enhance the contrast between the Ni and Ge. The tilt required for HRTEM was not achievable with the single tilt holder, also, during the anneal a lot of drift

Chapter 2. Experimental Methods

occurred which would have diminished any possibility of HRTEM during the anneal. The initial temperature and ramp rate was varied for the anneals. After each temperature increase, a stabilisation time of approximately 10 s was given. Smaller temperature increases, for example 10 degrees vs 100 degrees, resulted in less drift. Images were acquired at 1 minute intervals with 1 second acquisition time. After annealing, the sample was imaged in the double tilt holder again for HRTEM imaging in the same orientation as prior to annealing.

2.9 References

- 1 Biswas, S., Singha, A., Morris, M. A., Holmes, J. D. Inherent control of growth, morphology, and defect formation in germanium nanowires. *Nano Lett.* 12, 5654-5663, doi:10.1021/nl302800u (2012).
- 2 Biswas, S., O'Regan, C., Petkov, N., Morris, M. A., Holmes, J. D. Manipulating the growth kinetics of vapor-liquid-solid propagated Ge nanowires. *Nano Lett.* 13, 4044-4052, doi:10.1021/nl401250x (2013).
- 3 O'Regan, C., Biswas, S., O'Kelly, C., Jung, S. J., Boland, J. J., Petkov, N., Holmes, J. D. Engineering the growth of germanium nanowires by tuning the supersaturation of Au/Ge binary alloy catalysts. *Chem. Mater.* 25, 3096-3104, doi:10.1021/cm401281y (2013).
- 4 Biswas, S., O'Regan, C., Morris, M. A., Holmes, J. D. In-situ observations of nanoscale effects in germanium nanowire growth with ternary eutectic alloys. *Small* 11, 103-111, doi:10.1002/smll.201401240 (2015).
- 5 Gangnaik, A. S., Georgiev, Y. M., Collins, G., Holmes, J. D. Novel germanium surface modification for sub-10 nm patterning with electron beam lithography and HSQ resist. *J. Vac. Sci. Technol.* **awaiting publication** (2016).
- 6 Collins, G., Aureau, D., Holmes, J. D., Etcheberry, A., O'Dwyer, C. Germanium oxide removal by citric acid and thiol passivation from citric acid-terminated Ge(100). *Langmuir* 30, 14123-14127, doi:10.1021/la503819z (2014).
- 7 Ran, Y. Das, S., Hobbs, R., Georgiev, Y., Ferain, I., Razavi, P., Akhavan, N. D., Colinge, C. A., Colinge, J. Top-down process of germanium nanowires using EBL exposure of hydrogen silsesquioxane resist. *J. Ultimate Integr. Silicon* 145-148, doi: 10.1109/ulis.2012.6193378 (2012).

Chapter 2. Experimental Methods

- 8 Kelly, R. A., Holmes, J. D. & Petkov, N. Visualising discrete structural transformations in germanium nanowires during ion beam irradiation and subsequent annealing. *Nanoscale* 6, 12890-12897, doi:10.1039/c4nr04513k (2014).
- 9 Gangnaik, A. , Georgiev, Y. M., McCarthy, B., Petkov, N., Djara, V., Holmes, J. D. Characterisation of a novel electron beam lithography resist, SML and its comparison to PMMA and ZEP resists. *Microelectron. Eng.* 123, 126-130, doi:10.1016/j.mee.2014.06.013 (2014).
- 10 Hobbs, R. G., Schmidt, M., Bolger, C. T., Georgiev, Y. M., Fleming, P., Morris, M. A., Petkov, N., Holmes, J. D., Xiu, F. X., Wang, K. L., Djara, V., Yu, R., Colinge, J. P. Resist-substrate interface tailoring for generating high-density arrays of Ge and Bi₂Se₃ nanowires by electron beam lithography. *J. Vac. Sci. Technol. B* 30, doi:10.1116/1.4724302 (2012).
- 11 Law, J. T., Meigs, P. S. Rates of oxidation of germanium. *J. Electrochem. Soc.* 104, 154-159, doi:10.1149/1.2428524 (1957).
- 12 Prabhakaran, K., Ogino, T. Oxidation of Ge(100) and Ge(111) surfaces: an UPS and XPS study. *Surf. Sci.* 325, 263-271, doi:10.1016/0039-6028(94)00746-2 (1995).

Chapter 3

Investigating crystal
damage in germanium
nanowires due to ion
beam irradiation

3.1. Abstract

In this chapter we detail the application of electron microscopy to visualise discrete structural transitions incurring in single crystalline Ge nanowires upon Ga-ion irradiation and subsequent thermal annealing. Sequences of images for nanowires of varying diameters subjected to an incremental increase of the Ga-ion dose were obtained. Intricate transformations dictated by a nanowire's geometry indicate unusual distribution of the cascade recoils in the nanowire volume, in comparison to planar substrates. Following irradiation, the same nanowires were annealed in the TEM and corresponding crystal recovery followed in situ. Visualising the recrystallization process, we establish that full recovery of defect-free nanowires is difficult to obtain due to defect nucleation and growth.

3.2. Introduction

The irradiation of single crystal semiconductor substrates with energetic ion beams to introduce dopants has been developed extensively over the years, turning ion implantation into a standard doping technique in semiconductor manufacturing. Essentially, doping involves introducing an impurity into a substitutional or an interstitial site within the crystal which alters the electronic structure of the material. Ion implantation allows for accurate control of doping achieving precise dose, depth profile and uniformity. Single crystalline semiconductor nanowires require uniform and controllable doping for the creation of high performance devices such as field effect transistors (FETs),^{1,2} advanced sensors,^{3,4} photovoltaic⁵ and light emitter⁶ devices. Specifically, junctionless multigate FETs⁷ require a uniform distribution and

Chapter 3. Investigating crystal damage in germanium nanowires due to ion beam irradiation

high level of active dopants ($>1 \times 10^{19}$ atoms cm^{-2}) within perfectly crystalline source, gate and drain regions for reliable device performance, as demonstrated by both ab-initio simulations and experimental devices.⁸ With the aim to achieve enhanced control over the dopant levels and their uniform distribution, ion implantation has been applied to introduce dopants in Si and Ge nanowires.⁹⁻¹² In particular, Ge is a potential material for logic and optoelectronic devices due to its high hole and electron mobilities.¹³ The processing of bulk and particularly nanostructured Ge, including ion implantation and subsequent crystal recovery, requires further understanding.¹⁴⁻¹⁶

The interaction of the energetic ions with single crystal nanowires, in comparison to those in bulk substrates, can be considerably altered due to (i) ions impinging at different incident angles at a surface and (ii) abrupt termination of resultant atom recoils at nanowire surfaces.¹⁷ Whilst the range of ion interactions with bulk substrates, accumulated damage and impurity distribution are theoretically simulated through modelling nuclear collisions involving ions and recoiling atoms using SRIM (stopping and range of ions in matter) computer code¹⁸, the simulation of ion interactions in nanowires has recently been developed using an extension of the SRIM code; iradina (**ion range and damage in nanostructures**).^{17,19} Iradina is a static Monte Carlo simulation similar to SRIM, except the target shape can be defined within a nanoscale simulation volume.

Herein, electron microscopy data demonstrating the discrete structural transformations within single crystalline Ge nanowires upon ion irradiation is presented. Using a procedure based on a correlative analysis approach,²⁰ sequences

of TEM images following accumulated crystal damage at varying Ga-ion fluence and energy were acquired. A relationship between the initial nanowire geometry and crystal structure is identified.

3.3. Experimental Procedure

3.3.1 Instrumentation

The instruments used were an FEI Helios 600i NanoLab Dual Beam system (SEM/FIB) and a JEOL 2100 HRTEM equipped with a Gatan double tilt imaging holder. The dual beam FIB was used for all ion beam exposures using the Ga ion source. The double tilt holder was used for all high resolution TEM imaging.

3.3.2 Nanowires

Two methods were used for fabrication of nanowires used in this study – bottom-up and top-down. The bottom-up Ge nanowires were grown from Au NP seeds via a supercritical fluid process on Si substrates by Dr Subhajt Biswas, Dr Olan Lotty and Dr Colm O'Regan.¹⁵ Most of the nanowires were grown in the [111] direction, a small fraction of the nanowires were grown in the [211] direction, some of which contain intrinsic longitudinal defects in the [111] direction. The top-down Ge nanowires were defined on 50 nm GeOI substrates using HSQ (Hydrogen silsesquioxane) which is a negative tone electron beam resist. The EBL system used is a Raith eLINE operated at 10 kV by Dr Anushka Gangnaik.

3.3.3. Concurrent imaging platform

The carrier chip platform used for step-wise implantation/imaging of a specific nanowire is depicted schematically in Figure 3.1. Si chips with silicon nitride (SiN) membrane windows were used (Ted Pella), which were patterned using the FIB to label and open slits in the membrane. The patterning is of benefit for two reasons; the slits allow high resolution imaging of sections of the nanowire as well as facile navigation to locate the same nanowire. The parameters for patterning were: 7 lines 10 μm apart, 70 μm long and 0.5 μm wide for a nominal thickness of 300 nm with the Ga ion beam operating at 30 kV, 3 nA.

The nanowires were first imaged in the TEM where the growth direction, tilt required to achieve a low index zone axis and any intrinsic defects were identified. Nanowires that required no more than 10 degrees tilting in one direction, preferably along or perpendicular to their long axis, and fully crossed the opening were selected. The mounting of the membrane chips to the TEM holder was done with the aid of an optical microscope, ensuring the grid was mounted with a fixed orientation. This allows the nanowires to be imaged in the same orientation after each exposure. This accurate mounting method became more important as the nanowire reached a near/fully amorphous state. The grid was then transferred to the SEM/FIB for implantation. The nanowire was located using the SEM and then orientated (stage was rotated and moved in x- and y-directions) so that the nanowire length was at eucentric height when the stage was tilted, i.e. the nanowire was aligned left to right in the SEM. The eucentric height is the height where a point, here our nanowire, remains stationary when tilted. The coincidence point of the SEM and FIB is set at

Chapter 3. Investigating crystal damage in germanium nanowires due to ion beam irradiation

the eucentric height. The stage was tilted to 52° so the FIB is normal to the substrate surface. Most exposures were done at this tilt unless the tilt required for a nanowire in the TEM is $<2^\circ$, in this case the stage was tilted to 45° to avoid ion channelling. Ion channelling occurs if the ion beam direction is parallel to a crystal direction. The effect of ion channelling is a longer range of ion and hence a variation in implantation depth. The pattern for implantation was defined in the ion beam window as a Si mill rectangle: $10 \times 10 \mu\text{m}^2$ area, 125 ns dwell time, 1 pass and with a total time of 0.316 s to achieve a dose of 1.9×10^{13} ions cm^{-2} , operating at 30 kV (or 5 kV), 9.7pA (10pA aperture at 5kV). The carrier chip was then transferred back to the TEM in the same orientation to image the nanowire after doping. The concurrent implantation/imaging steps were repeated multiple times to build up the step-wise increase in the dose. The maximum implantation dose in our studies was 1.14×10^{14} ions cm^{-2} which corresponds to 6 successive steps.

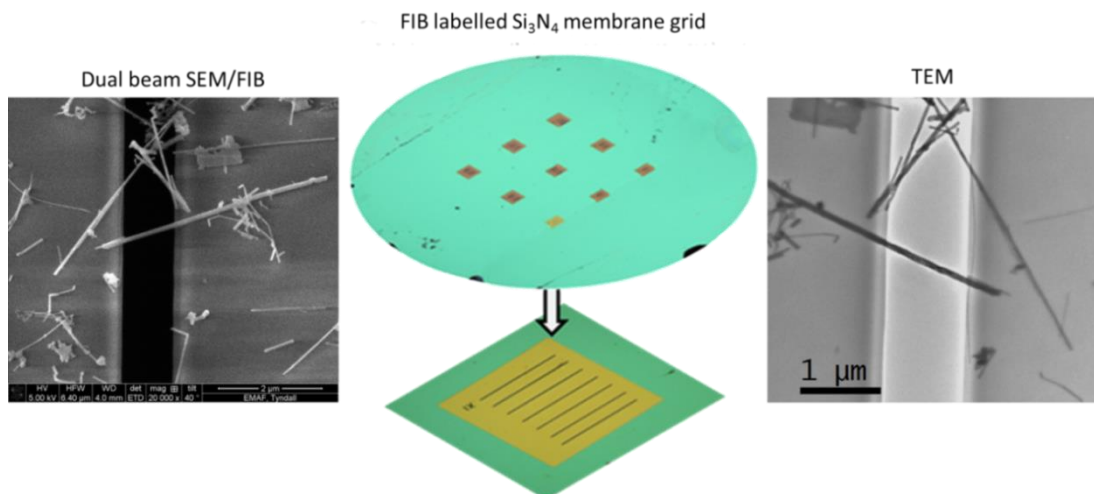


Figure 3.1. Overview of platform for correlative imaging of nanowire on Si₃N₄ membrane grid.

3.3.4. Iradina (ion range and damage in nanostructures)

Iradina was used to simulate ion beam irradiation in Ge nanowires. The material of the wire was defined as Ge and the surrounding material set as vacuum. For this experimental procedure the nanowire was defined as a cylinder with a varied diameter, 65 nm, 45 nm or 25nm. The accelerating voltage was set to 5 kV or 30 kV for the Ga ion source. A section of the nanowire was defined by the periodic boundary conditions (PBC), essentially defining a 2 dimensional cross section of the nanowire, which in turn is divided into a number of cells (defined by the user). For the results presented here, the PBC was set at $80 \times 80 \text{ nm}^2$, with the individual cells set at $0.5 \times 0.5 \text{ nm}^2$. The ion beam direction is set orthogonal to the nanowire length as the crystallinity of the material is disregarded due to random phase approximation (RPA) of the target atoms so any ion channeling in the crystal is not accounted for.

3.4. Results and Discussion

3.4.1. 30 kV single exposure irradiation

In Figure 3.2 cross-sections of three different nanowires are presented, all approximately 45 nm in diameter, subjected to an increasing Ga-ion dose at 30 kV. The extent of crystal damage in the nanowires at the fixed implantation energy can be directly related to the dose used. At a fluence of $1.9 \times 10^{13} \text{ ions cm}^{-2}$ (Figure 3.2 a and d), the arc of crystal damage shows large contrast variations due to lattice distortions resulting from clustering of point defects. Small amorphous regions (3 - 5 nm in size) were seen at the nanowire surface imaged at lattice resolution, imaged

with the electron beam perpendicular to the longitudinal direction of the nanowire (Figure 3.3). With the increase of the implantation fluence by 2 and 3 times (Figure 3.2 b -and c), further increase of the top surface damage depth from approximately 18 nm to 25 and 34 nm, respectively, in the form of full amorphisation towards the interior (across the diameter) of the nanowires was observed.

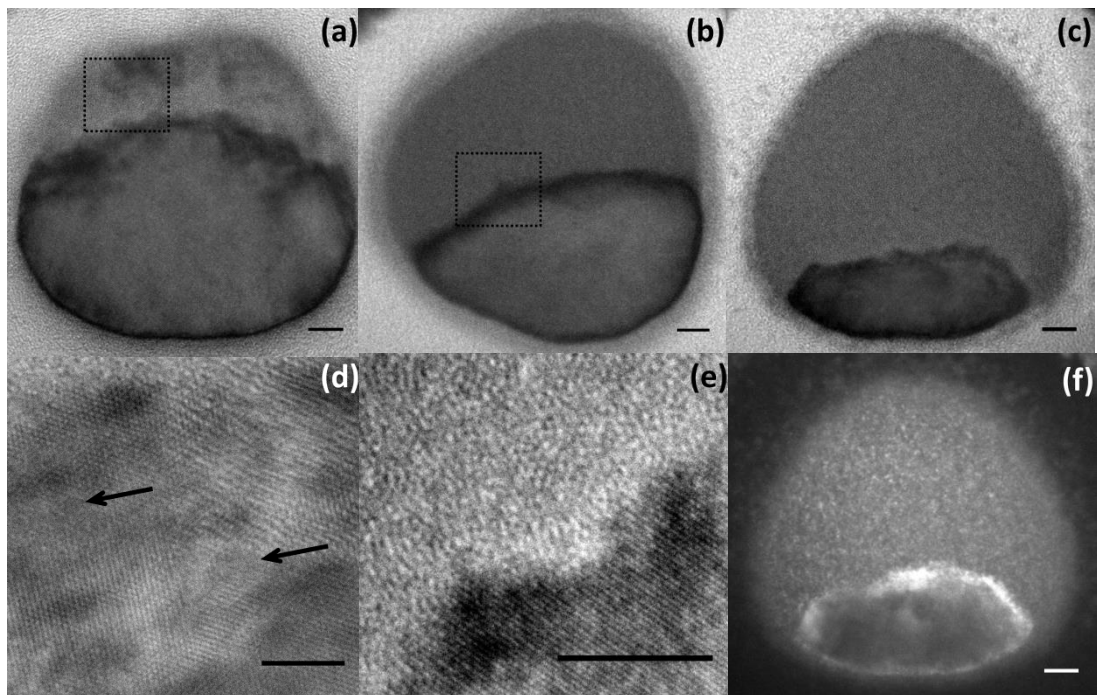


Figure 3.2. Cross-sectional TEM images of different Ge nanowires of approximately 45 nm in diameter after irradiation at 30 kV with increasing Ga-ion doses of (a) 1.9×10^{13} , (b) 3.8×10^{13} and (c) 5.7×10^{13} ion cm^{-2} . (d) and (e) lattice resolution TEM images taken from the marked areas in (a) and (b), respectively. (f) Dark field TEM image of the same nanowire as in (c). In all images, the direction of the ion flux is from the top and the cross-sections were imaged in the [111] zone direction. Arrows in (d) mark small amorphous pockets. Scale bar for all images is 5 nm.

Additionally, Figure 3.2 demonstrates gradual decrease in the roughness of the amorphous to crystalline interface as a function of increasing fluence as the amorphisation depth reaches the maximum range of the ion in the material.

Chapter 3. Investigating crystal damage in germanium nanowires due to ion beam irradiation

Measuring from the top and centre of the nanowire in Figure 3.2 c, this depth for a 30 kV Ga ion beam in Ge is approximately 32 nm. In comparison to the experimental results for ion irradiation of Ge (001) substrates, the maximum depth was approximately 35 nm for a dose of 1.45×10^{14} ions cm^{-2} for a 30kV ion beam. Intrinsic (111) stacking fault defects present in some of the Ge nanowires (Figure 3.5 a) produced during growth showed a slight susceptibility to damage at the grain boundary but this was a minimal variation and cannot be fully attributed to the intrinsic defect present. Other nanowires presented in Figure 3.5 b-d also show a non-uniform crystalline-amorphous (c/a) interface. Importantly, the analysis of the crystal damage was done post-factum, with no account of the initial nanowire structure and orientation towards the incoming ion beam. Conventionally, when implanting planar substrates the orientation of the incoming ion beam to the crystal is known, set at an angle (about 7 degrees off normal direction) to minimize unwanted channeling effects.

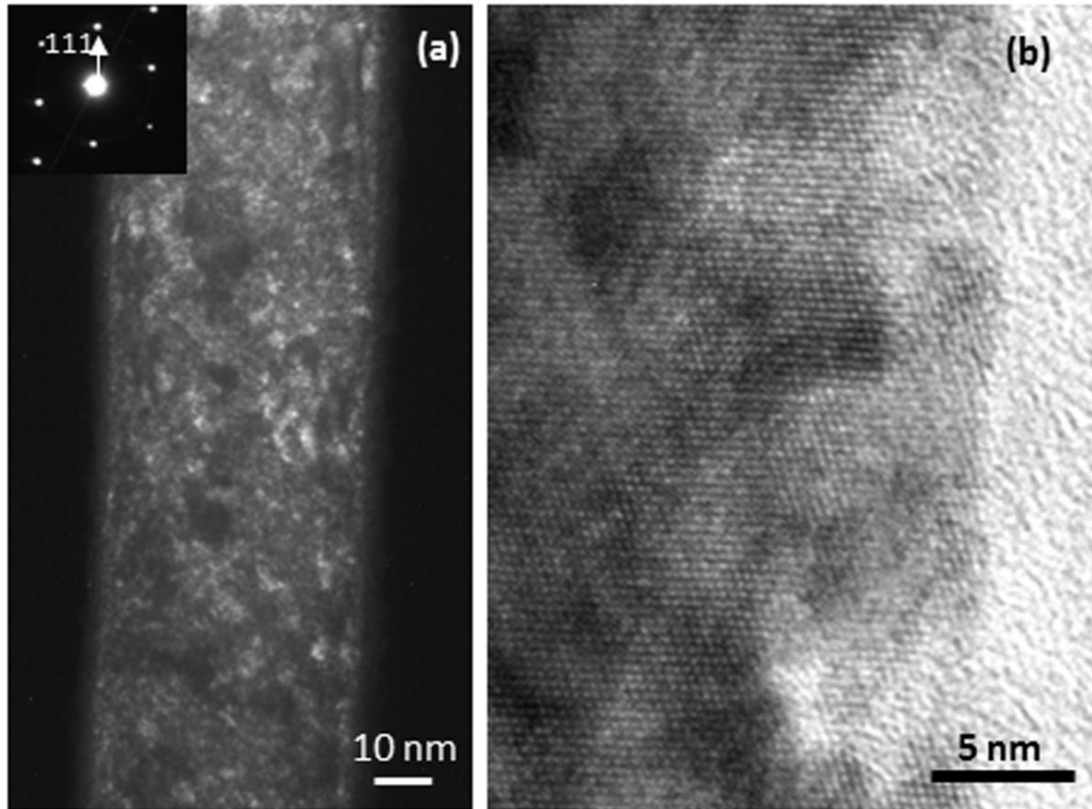


Figure 3.3. Consecutive 30kV Ga ion irradiations of a 50 nm diameter Ge nanowire 6 degrees off the [110] zone direction at a fluence of 1.9×10^{13} ion cm^{-2} . (a) Dark field imaging taken under $g, 2g$ with $g = 220$ conditions. (b) Corresponding lattice resolution image taken in the [110] zone direction at the nanowire side surface. After further irradiation; The white spots in the dark field images are due to roughness of the surface but could also be Ga clusters embedded in the NW.

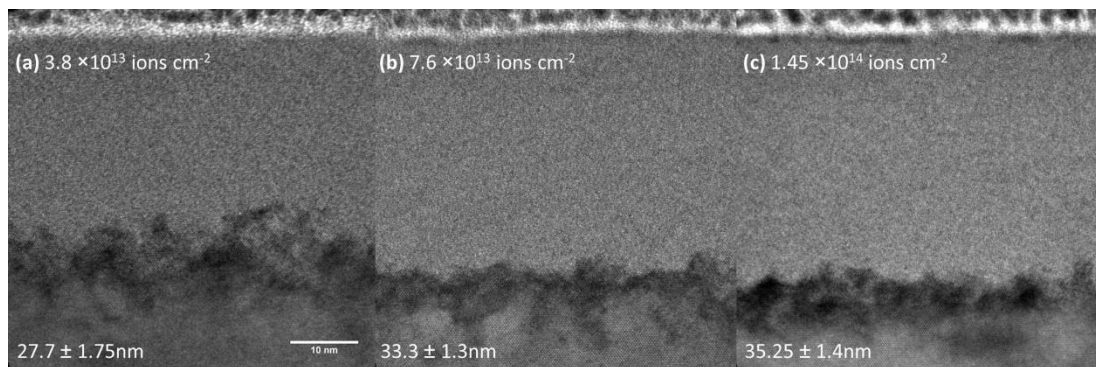


Figure 3.4. Cross sectional TEM of Ge(001) substrate exposed to Ga-ion implantations 7 degrees off the normal direction at increasing fluences for 30 kV. Doses and measured average thicknesses of amorphous layers are given in the insets.

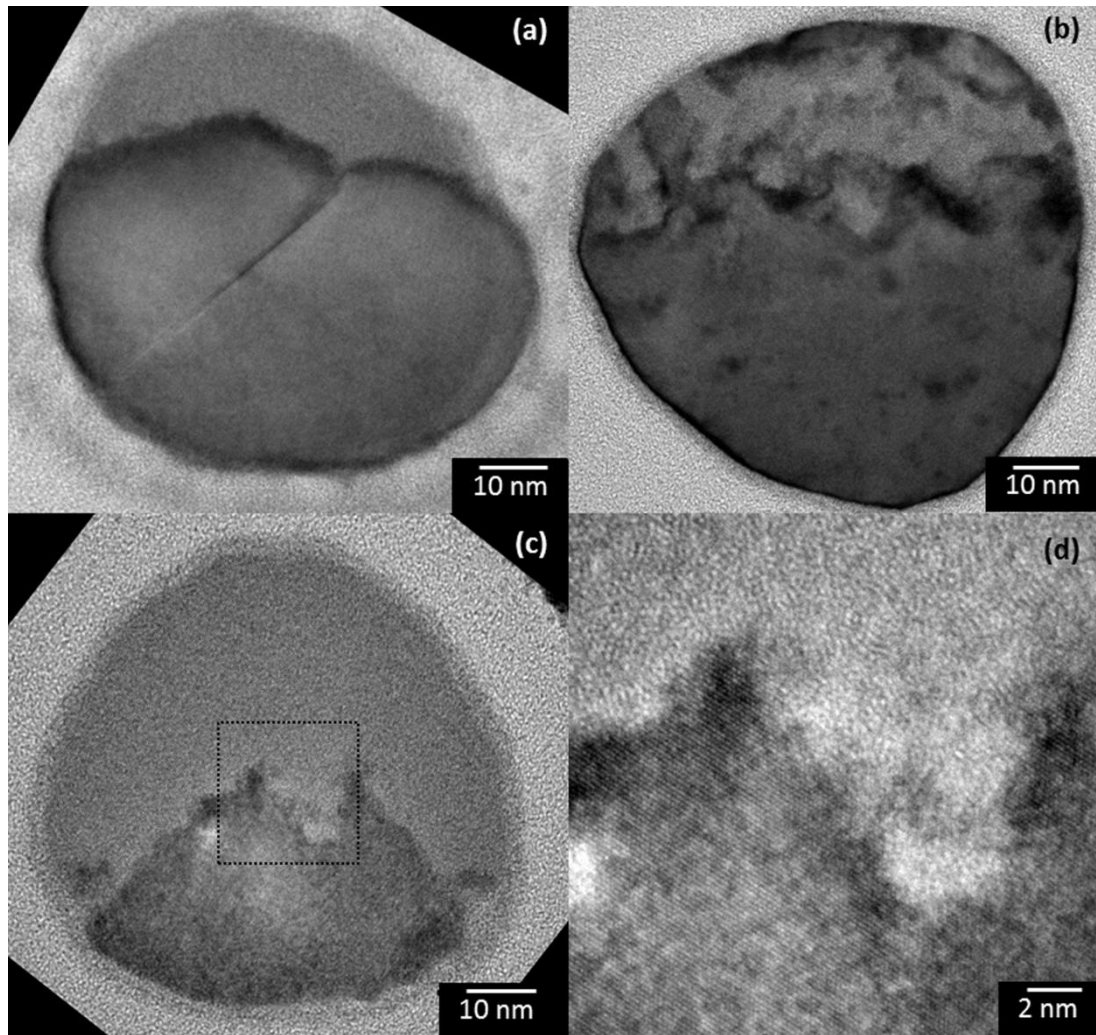


Figure 3.5. Cross-sectional TEM images of different nanowires subjected to Ga-ion implantations (a-d) at 30kV with the incoming irradiation from the top. Excluding the nanowire in (a), all nanowires were defect free and grown in the [111] direction. (a) 64 nm Ge nanowire grown along the [211] direction irradiated with a fluence of 3.8×10^{13} ion cm^{-2} , featuring intrinsic stacking fault defects along the (111) set of planes. (b) 74 nm diameter Ge nanowire irradiated with a fluence of 1.9×10^{13} ion cm^{-2} , featuring amorphous pockets within a mostly crystalline structure. (c) 60 nm nanowire irradiated with a fluence of 7.6×10^{13} ion cm^{-2} featuring extended but not full amorphisation leaving crystalline domains towards the middle/bottom of the nanowire cross-section. (d) Lattice resolution image of the area marked in (c), demonstrating an uneven c/a interface.

3.4.2. Concurrent stepwise 30 kV irradiation

A procedure to accurately follow the evolution of crystal damage in nanowires was developed based on a correlative analysis approach,²⁰ using a carrier chip platform with markers that facilitated exchange between the TEM and FIB/SEM instruments (Figure 3.1). Figure 3.6 represents the evolution of damage build-up in a 38 nm Ge nanowire with a step-wise increase in the Ga-ion dose at 30 kV, starting at a minimum fluence (step) of 1.9×10^{13} ions cm^{-2} . The nanowire was first imaged in the TEM to obtain information about crystallinity and its orientation towards the incoming electron beam. Although most of the examined nanowires were defect free and grown along the [111] direction, in order to demonstrate the capabilities of our visualization methodology a [211] grown Ge nanowire with a set of stacking fault defects along the [111] direction was selected. A cross-section of an equivalent nanowire, having the same type of intrinsic defect and growth orientation (but with a larger diameter) is presented in Figure 3.5 a. The carrier chip was first tilted approximately 8 degrees (in one direction) to image the nanowire in the [110] zone direction. After transferring to the SEM/FIB instrument the sample was imaged first with the SEM to locate and orient the carrier chip. After tilting the stage to 52 degrees (ion beam normal to the carrier chip surface) successive ion irradiation was performed at a known tilt angle, i.e. 8 degrees away from the (110) zone axis.

Following ion implantation, the nanowire sample was transferred back to the TEM and imaged along the same zone axis to observe sustained structural transformations. These sequences were repeated several times to build up the implantation dose and obtain images monitoring the consecutive transformations. At the lowest Ga-ion

Chapter 3. Investigating crystal damage in germanium nanowires due to ion beam irradiation

fluence used (Figure 3.6 b) lattice distortions as well as amorphous regions (about 5 nm in size) were observed in comparison to the initial single crystalline nanowire. By further multiplying the initial ion fluence of 1.9×10^{13} ions cm^{-2} by 2, 3 and 4 times the volume of amorphous regions increased, breaking the stacking fault planes at the centre of the nanowire and transforming almost the whole volume of the nanowire amorphous. These transformations were unevenly distributed along the nanowire length. At the highest fluence used, the resultant amorphous nanowire contained isolated crystalline domains in the sub-10 nm range, with the same orientation as the initial single crystal structure, as seen from the lattice resolution image (Figure 3.6 f); some slightly misoriented domains were also observed. Taking into account the cross-sectional data (Figure 3.2 and Figure 3.5), one can envision that these crystalline islands would be predominantly located towards the middle and bottom (bottom is defined as the side opposite to the incoming ion beam) of the nanowire. These data collaborate very well to the simulations by iradina (Figure 3.7 a-d), where the lowest number of atom displacements for a 45 nm nanowire is in the middle and bottom of the nanowire cross-section.

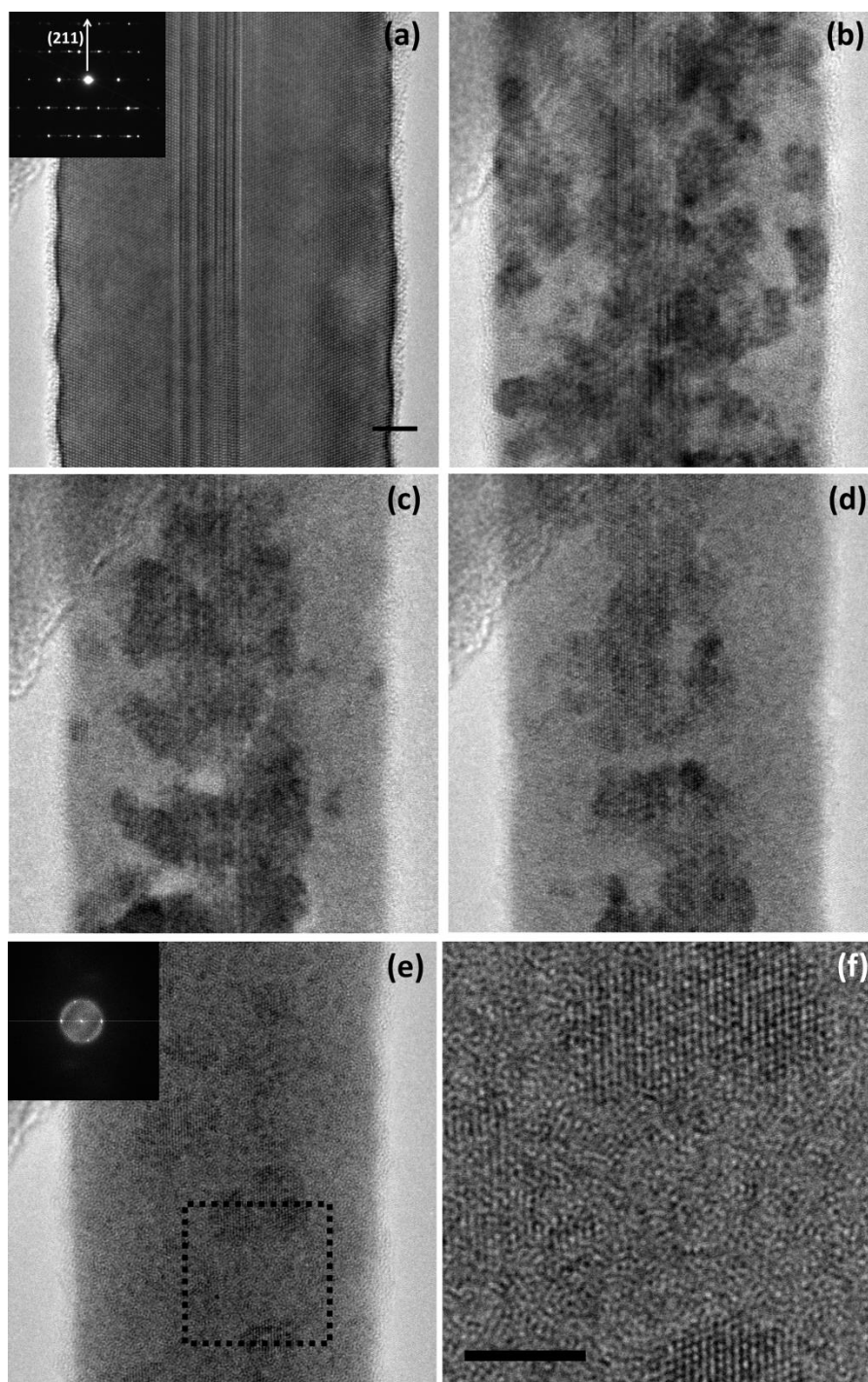


Figure 3.6. Step-wise irradiation of a 38 nm diameter Ge nanowire with a 30 kV Ga-ion beam. (a) Initial nanowire before irradiation imaged close to the [110] zone axis, inset demonstrating complex SAED due to longitudinal (111) stacking fault defect. (b-e) Images of the same area taken close to the same zone direction after irradiation with increasing fluence of (b) 1.9×10^{13} , (c), 3.8×10^{13} (d) 5.7×10^{13} and (e) 7.6×10^{13} ion cm^{-2} . All images were acquired at the same magnification. (f) Inset of (e) shows FFT of region marked. Lattice resolution TEM image of the marked area in (e), demonstrating crystal domains orientated in the same [110] direction as the initial nanowire. Scale bar for all images is 5 nm.

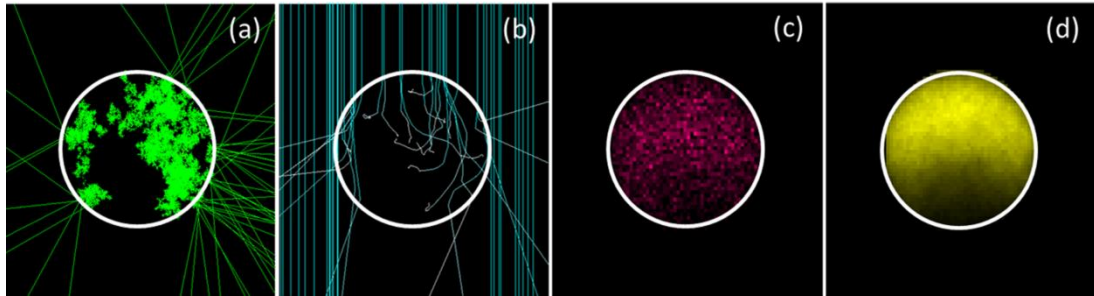


Figure 3.7. Irradina maps of (a) cascade recoils, (b) ion paths, (c) implanted ions and (d) atom displacements based on a cylindrical Ge nanowire with a diameter of 45 nm irradiated by a 30 kV Ga ion beam orthogonal to the nanowire.

The cascade recoils (Figure 3.7 a) show the resultant collisions which occur within the NW. The ion paths (Figure 3. b) show the path of the ions as they enter, and leave, the NW volume. Both the cascade recoils and ions paths illustrate how the ions and atoms from NW can easily be expelled and hence resulting in a lower concentration of implanted ions as well as sputtering events at NW surface. The implanted ion map (Figure 3.7 c) shows the estimated distribution of ions within the NW. The atom displacements map (Figure 3.7 d) shows the distribution of displacement of atoms within the volume, which can be used to estimate the damage and amorphisation in the NW.

In comparison, a larger diameter Ge nanowire (64 nm, grown along [111] direction with prominent stacking fault defects along [11-1] direction) implanted with successive Ga-ion doses of 1.9×10^{13} to 7.6×10^{13} ions cm^{-2} , imaged along the (110) zone axis, displayed an increase in lattice distortions and build-up of amorphous pockets, increasing in size from 3 to 10 nm at the side surfaces (Figure 3.8). For this large diameter nanowire, extended amorphisation was not observed even at a dose as high as 1.1×10^{14} ions cm^{-2} .

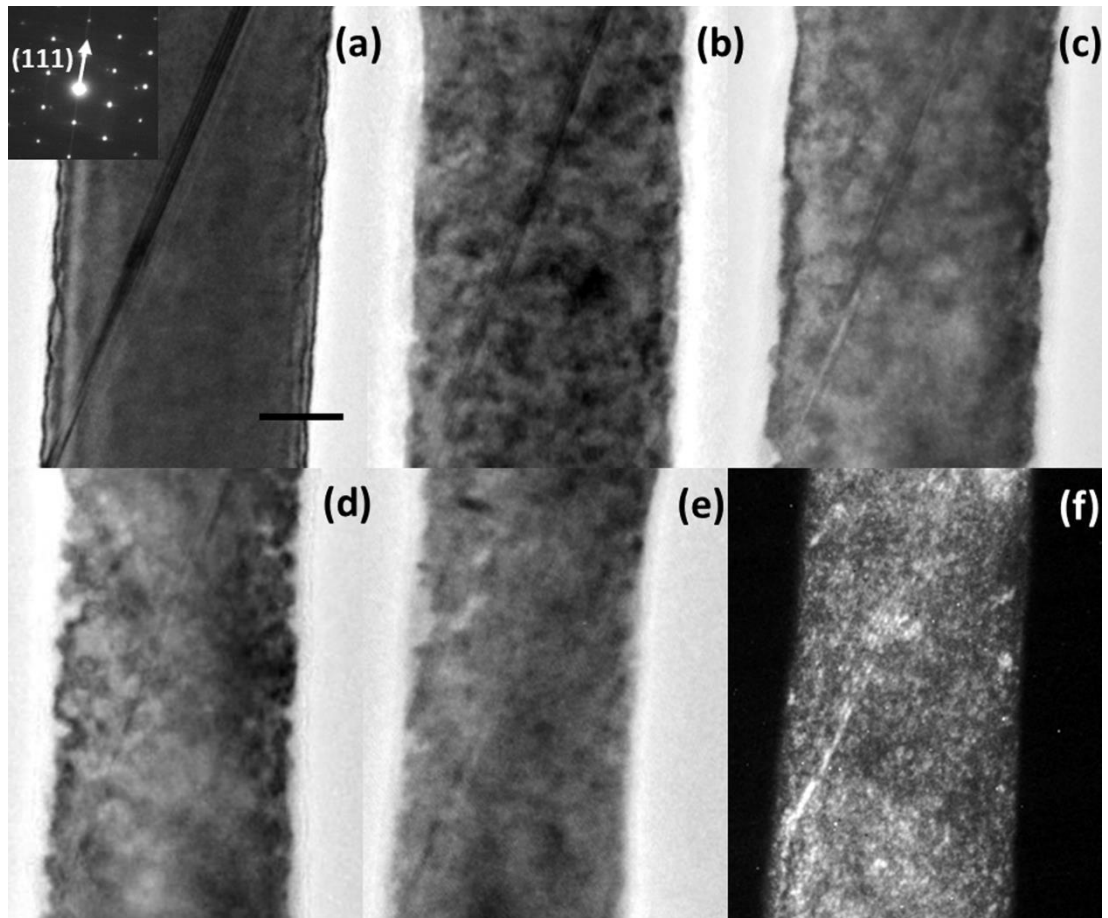


Figure 3.8. Consecutive 30 kV Ga-ion irradiations of a 64 nm diameter Ge nanowire tilted approximately 3 degrees off the [110] zone axis during the exposures. (a) Initial nanowire before irradiation imaged in the [110] zone axis, inset SAED pattern taken at a region without the defect shown. Images of the same area taken in the same zone axis after irradiation, with an increasing fluence of (b) 1.9×10^{13} , (c) 3.8×10^{13} , (d) 5.7×10^{13} and (e) 7.6×10^{13} ion cm^{-2} . All images are at the same magnification. (f) Weak beam dark field image taken under $g, 2g = 220$ conditions highlights most of the stacking fault defects are still present after irradiation. Scale bar for all images is 20 nm.

Using this method, the evolution of crystal damage was monitored for 10 different nanowires with diameters ranging between 25 and 65 nm for a step-wise increase of the Ga-ion dose at 30 kV from 1.9×10^{13} to 1.1×10^{14} ions cm^{-2} . For the largest (>50 nm) diameter nanowires, crystal damage scaled with Ga-ion fluence but full amorphisation was not observed even at the highest fluence used. For the nanowires in the 30-50 nm range the evolution of the crystal damage was equivalent to the

sequence of images in Figure 3.6. Whereas the nanowires in the 25-30 nm range were almost fully amorphised (with remaining <5 nm crystallites) even at the lowest fluence (1.9×10^{13} ions cm^{-2}) used (Figure 3.9, and Figure 3.10 a and b).

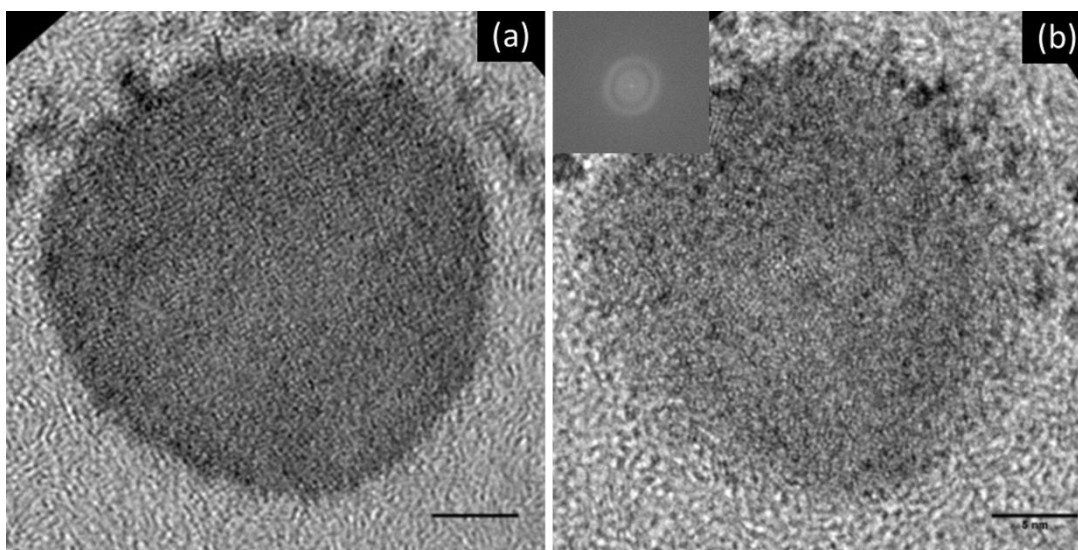


Figure 3.9. (a) and (b) Cross-sectional TEM images at different tilt angles of almost fully amorphised 25 nm nanowire that was subjected to 30 kV Ga-ion implantation at a fluence of 1.9×10^{13} ions cm^{-2} . Initially the nanowire was imaged along the growth direction (image on the left) which was determined by using the electron diffraction of the Si carrier wafer. Image (b) is after 28 degrees tilt in one-direction. Selected area electron diffraction patterns for both nanowires showed attenuated amorphous rings.

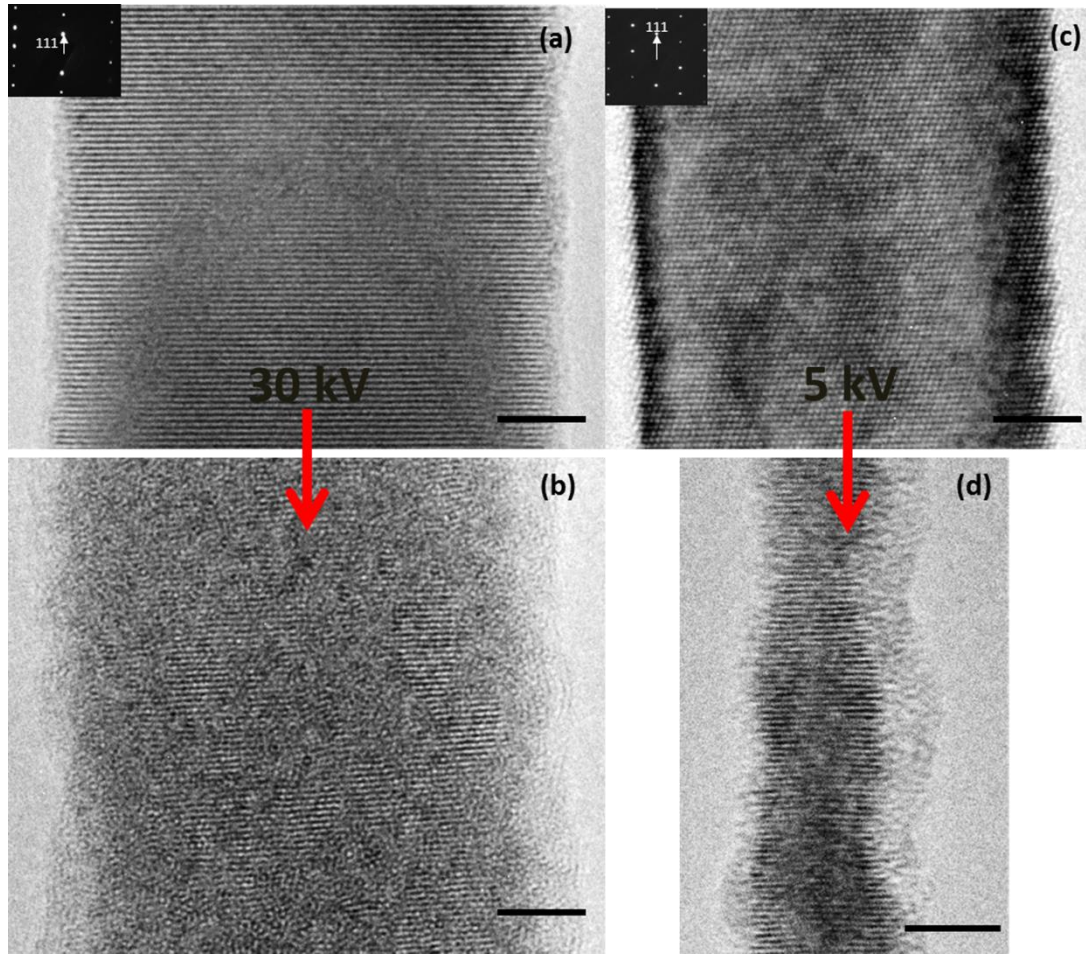


Figure 3.10. 30 kV Ga ion irradiation of a 25 nm diameter Ge nanowire with a beam tilted to about 3 degrees away from the [210] zone direction. (a) Before irradiation and (b) after irradiation at 1.9×10^{13} ion cm^{-2} . Lattice resolution images are taken close to the [210] zone direction. 5 kV Ga-ion irradiation of a 20 nm diameter Ge nanowire with the beam tilted to about 5 degrees away from the [110] zone direction; (c) before irradiation and (d) after irradiation at 7.6×10^{13} ion cm^{-2} . Lattice resolution images are taken close to the [110] zone direction. Scale bars in all images are 5 nm.

3.4.3. 5 kV irradiation

To examine the possibility of lower energy implantations and corresponding evolution of the crystal damage in small diameter nanowires (<25 nm), ion implantations at 5 kV were performed. Due to the drastically limited range of interactions of Ga-ions with Ge at 5 kV, the largest number of atom displacements

was predicted from Iradina at approximately 5 – 8 nm from the surface (Figure 3.11). The decreased range due to reduced accelerated voltage is shown for bulk substrates in Figure 3.12. Hence step-wise increase in the ion fluence can be used to build-up crystal damage in analogy to 30 kV implantations in Ge nanowires with diameters >30 nm. Figure 3.13. presents a sequence of images for a 22 nm Ge nanowire subjected to an increasing Ga-ion fluence at 5 kV. Although the damage build-up followed a similar trend as for the 30 kV implantations, i.e. amorphisation starting at the nanowire surface after forming defects, there are some morphological differences. The increase in ion fluence resulted in a reduced nanowire diameter, forming an undulated surface, while the remaining crystalline nanowire interior appeared less distorted with reduced number of domains containing crystal defects, in comparison to the 30 kV implantations. The amorphisation was predominantly localised at the nanowire surface and progressed with gradual decrease of the crystalline core of the nanowire from 20 to $8 \text{ nm} \pm 3 \text{ nm}$ for the dose increase of 1.9 to $5.7 \times 10^{13} \text{ ions cm}^{-2}$. A further increase in the ion fluence resulted in further deterioration of the nanowire due to amorphisation and subsequent knock-out damage from the nanowire surface (Figure 3.13 d).

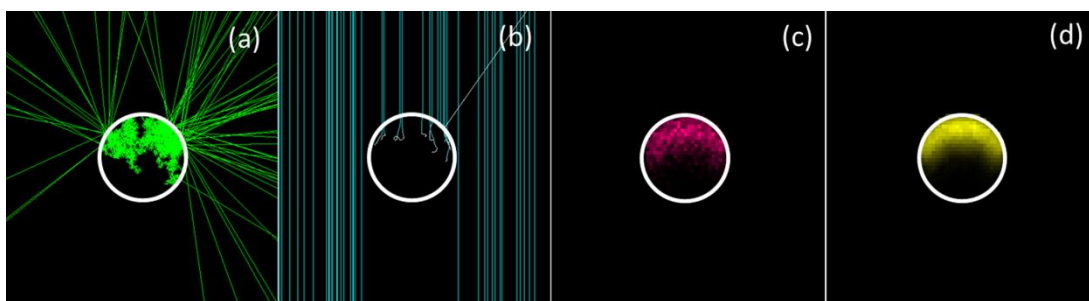


Figure 3.11. Iradina maps of (a) cascade recoils, (b) ion paths, (c) implanted ions and (d) atom displacements based on a cylindrical Ge nanowire with a diameter of 45 nm irradiated by a 5 kV Ga ion beam orthogonal to the nanowire.

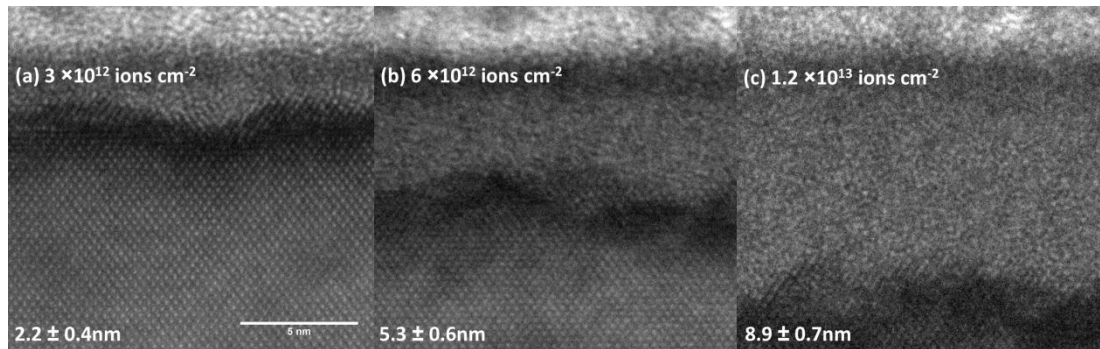


Figure 3.12. Cross sectional TEM of Ge(001) substrate exposed to Ga-ion implantations 7 degrees off the normal direction at increasing fluences at 5 kV. Doses and measured average thicknesses of amorphous layers are given in the insets.

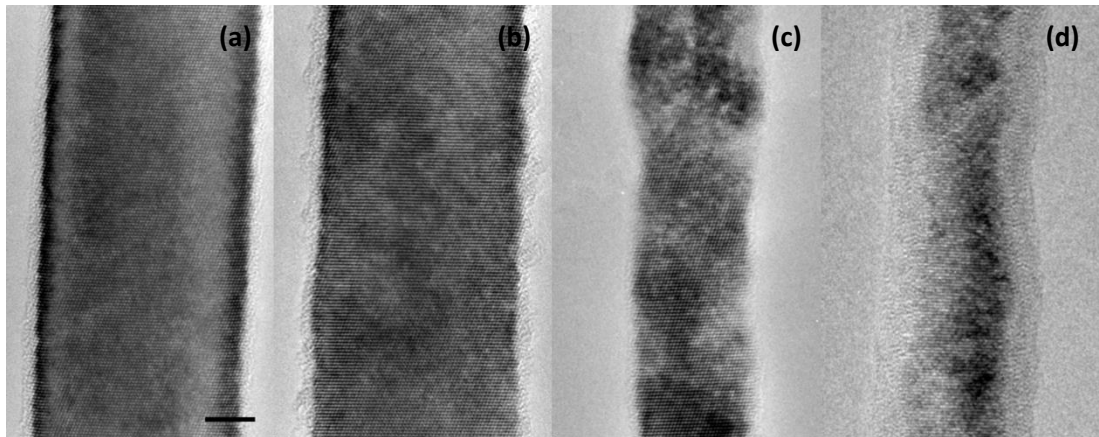


Figure 3.13. Step-wise irradiation of a 22 nm diameter Ge nanowire with a 5 kV Ga-ion beam. (a) Initial nanowire before irradiation imaged close to the [110] zone axis. (b–e) Images of the same area taken in the same zone direction after irradiation with increasing fluence of 1.9×10^{13} , 3.8×10^{13} , 5.7×10^{13} and 7.6×10^{13} ion cm^{-2} . All images were acquired at the same magnification. Scale bar for all images is 5 nm. The direction of the incoming Ga-ion beam during implantation was 5 degrees off the [110] direction.

Similar to flat substrates (Figure 3.4 and Figure 3.12), the depth of crystal damage in the Ge nanowires scaled with the Ga-ion energy and fluence. However, in our study we recorded several differences that are solely related to nanowires. Firstly, the amount and profile of the incurred ion beam damage, at a set energy and fluence, is strongly dependent on nanowire size. The thickness of the damage arc is not conformal; it is much wider at the top of the nanowire cross-section where the ion

Chapter 3. Investigating crystal damage in germanium nanowires due to ion beam irradiation

beam is normal to the nanowire surface and narrower where the beam is at an oblique or parallel direction. In contrast, flat substrates normally exhibit uniform crystal damage across the whole irradiated surface. This non-conformal damage profile, which is in agreement with the atom displacement maps obtained by iradina, can be understood by looking at the cascade recoils in the nanowires (Figure 3.7). Cascade recoils initiated by the ion beam that are normal to the nanowire surface, i.e. entering at the top/middle of the nanowire, terminate in the bulk of the nanowire after losing their energy. In comparison, the recoils that are localised near the side surfaces (absent in flat substrates) can exit the volume of the nanowire thus diminishing the probability of atom displacements. Specifically at lower energies, e.g. 5 kV, the range of cascade recoils is concentrated in approximately 5 - 8 nm of the nanowire surface. Hence, a large implantation dose will not only induce extended amorphisation in these regions but will also promote greater knock-out damage, as seen in our experiments. The unusual distribution of the cascade recoils in nanowires, in comparison to planar substrates, can be used to explain the observed uneven distribution of amorphisation pockets along the length of the nanowires. Iradina does not predict any variations in the ion interactions in the axial direction of the nanowires as the periodic boundary conditions along this direction are kept constant.

On the other hand, there are aspects of the crystalline to amorphous transition in nanowires that are similar to planar Ge substrates. The formation of the amorphous phase in Si and Ge substrates due to ion bombardment has been associated with the formation of a large number of point defects, including local rearrangement of bonds

(interstitial-vacancy pair (Frenkel) defects), which when reaching a critical density spontaneously relax towards the amorphous phase.²¹ At low Ga-ion fluence, lattice distortions in the form of large numbers of clustered point defects²² and amorphous pockets which at higher fluences merged into extended amorphous regions. The spatial distribution of these regions is dictated by the geometry of the nanowires leading to an unusual, in comparison to planar substrates, distribution of the collision cascades. The transformation process described herein is different to the crystalline to amorphous transitions observed previously by in-situ TEM for single crystalline nanowires under incremental increase of mechanical (bending) stress. During these mechanical influences the formation and movement of dislocations towards the region that is transformed into the amorphous phase has been observed.²³

3.5. Conclusions

In this chapter, a method for the mechanistic understanding of ion beam induced damage in NWs has been presented. We have described the application of electron microscopy to study the crystalline-amorphous transition in single crystal Ge nanowires upon Ga-ion irradiation. Sequences of images for nanowires of varying diameters subjected to an incremental increase of the Ga-ion dose were obtained. Intricate transformations dictated by a nanowire's geometry indicate an unusual distribution of the cascade recoils in the nanowire volume, in comparison to planar substrates. Our findings will have large implications in designing ion beam doping of Ge nanowires for electronic devices but also for other devices that use single

crystalline nanostructured Ge materials such as thin membranes, nanoparticles and nanorods.

From the analysis of sustained structural transformations upon ion irradiation we establish that there are morphological differences in the Ga-ion beam damage of Ge nanowires suggesting that critical defect densities, corresponding critical damage energy, knock-out damage and dynamic annealing effects are altered as compared to those known for planar substrates. We postulate that the obtained ion implantation data using Ga-ion beams as a probe to induce structural transformations can be used to comprehend the final degree of damage in Ge nanowires but also in other nanostructured Ge materials induced by any heavy ions. Critical damage energy (5eV/at) in Ge substrates is found to be independent of the density of the cascades induced by different ions and energies.^{24,25} A critical damage energy density model for ion implantation in nanostructures is important to establish and compare with bulk but this is beyond the scope of this study. A variation in energy, dopant atom, temperature and also dimensions of a nanostructure would be required for a sufficient study.

3.6. References

- 1 Huang, Y., Duan, X. F., Cui, Y., Lauhon, L. J., Kim, K. H., Lieber, C. M. Logic gates and computation from assembled nanowire building blocks. *Science* 294, 1313-1317, doi:10.1126/science.1066192 (2001).
- 2 Cui, Y., Duan, X. F., Hu, J. T. & Lieber, C. M. Doping and electrical transport in silicon nanowires. *J. Phys. Chem. B* 104, 5213-5216, doi:10.1021/jp0009305 (2000).

- 3 Michel, J., Liu, J. & Kimerling, L. C. High-performance Ge-on-Si photodetectors. *Nat. Photonics* 4, 527-534, doi:10.1038/nphoton.2010.157 (2010).
- 4 Cui, Y., Wei, Q. Q., Park, H. K. & Lieber, C. M. Nanowire nanosensors for highly sensitive and selective detection of biological and chemical species. *Science* 293, 1289-1292, doi:10.1126/science.1062711 (2001).
- 5 Tian, B., Zheng, X., Kempa, T. J., Fang, Y., Yu, N., Yu, G., Huang, J., Lieber, C. M. Coaxial silicon nanowires as solar cells and nanoelectronic power sources. *Nature* 449, 885-U888, doi:10.1038/nature06181 (2007).
- 6 Yan, R., Gargas, D. & Yang, P. Nanowire photonics. *Nat. Photonics* 3, 569-576, doi:10.1038/nphoton.2009.184 (2009).
- 7 Ferain, I., Colinge, C. A. & Colinge, J.-P. Multigate transistors as the future of classical metal-oxide-semiconductor field-effect transistors. *Nature* 479, 310-316, doi:10.1038/nature10676 (2011).
- 8 Colinge, J. P., Kranti, A., Yan, R., Lee, C. W., Ferain, I., Yu, R., Akhavan, N. D., Razavi, P. Junctionless Nanowire Transistor (JNT): Properties and design guidelines. *Solid-State Electron.* 65-66, 33-37, doi:10.1016/j.sse.2011.06.004 (2011).
- 9 Fukata, N., Takiguchi, R., Ishida, S., Yokono, S., Hishita, S., Murakami, K. Recrystallization and Reactivation of Dopant Atoms in Ion-Implanted Silicon Nanowires. *ACS Nano* 6, 3278-3283, doi:10.1021/nn300189z (2012).
- 10 Das Kanungo, P., Koegler, R., Nguyen-Duc, K., Zakharov, N., Werner, P., Goesele, U. Ex situ n and p doping of vertical epitaxial short silicon nanowires by ion implantation. *Nanotechnology* 20, doi:10.1088/0957-4484/20/16/165706 (2009).
- 11 Colli, A., Fasoli, A., Ronning, C., Pisana, S., Piscanec, S., Ferrari, A. C. Ion beam doping of silicon nanowires. *Nano Lett.* 8, 2188-2193, doi:10.1021/nl080610d (2008).
- 12 Das Kanungo, P., Koegler, R., Zakharov, N., Werner, P., Scholz, R., Skorupa, W. Characterization of Structural Changes Associated with Doping Silicon Nanowires by Ion Implantation. *Cryst. Growth Des.* 11, 2690-2694, doi:10.1021/cg200108u (2011).
- 13 Haynes, J. R. & Shockley, W. The mobility and life of injected holes and electrons in germanium. *Phys. Rev.* 81, 835-843, doi:10.1103/PhysRev.81.835 (1951).
- 14 Duffy, R., Shayesteh, M., McCarthy, B., Blake, A., White, M., Scully, J., Yu, R., Kelleher, A. M., Schmidt, M., Petkov, N., Pelaz, L., Marques, L. A. The curious case of thin-body Ge crystallization. *Appl. Phys. Lett.* 99, doi:10.1063/1.3643160 (2011).

- 15 Biswas, S., O'Regan, C., Petkov, N., Morris, M. A. & Holmes, J. D. Manipulating the Growth Kinetics of Vapor-Liquid-Solid Propagated Ge Nanowires. *Nano Lett.* 13, 4044-4052, doi:10.1021/nl401250x (2013).
- 16 Yu, R., Georgiev, Y. M., Das, S., Hobbs, R. G., Povey, I. M., Petkov, N., Shayesteh, M., O'Connell, D., Holmes, J. D., Duffy, R. Junctionless nanowire transistor fabricated with high mobility Ge channel. *Phys. Status Solidi RRL* 8, 65-68, doi:10.1002/pssr.201300119 (2014).
- 17 Borschel, C. & Ronning, C. Ion beam irradiation of nanostructures - A 3D Monte Carlo simulation code. *Nucl. Instrum. Methods Phys. Res., Sect. B* 269, 2133-2138, doi:10.1016/j.nimb.2011.07.004 (2011).
- 18 Ziegler, J. Particle interactions with matter, <<http://www.srim.org/>>
- 19 C Borschel, C. R. Ion beam irradiation of 3D nanostructures-a new Monte Carlo simulation code, <www.iradina.de> (2011).
- 20 Stiegler, J. M., Tena-Zaera, R., Idigoras, O., Chuvilin, A. & Hillenbrand, R. Correlative infrared-electron nanoscopy reveals the local structure-conductivity relationship in zinc oxide nanowires. *Nat. Commun.* 3, doi:10.1038/ncomms2118 (2012).
- 21 Claverie, A., Vieu, C., Faure, J. & Beauvillain, J. Cross-sectional high-resolution electron microscopy investigation of argon-ion implantation-induced amorphization of silicon. *J. Appl. Phys.* 64, 4415-4423, doi:10.1063/1.341264 (1988).
- 22 Rettig, R., Steuer, S. & Singer, R. F. Diffusion of Germanium in Binary and Multicomponent Nickel Alloys. *J. Phase Equilib. Diffus.* 32, 198-205, doi:10.1007/s11669-011-9853-6 (2011).
- 23 Decoster, S. & Vantomme, A. Implantation-induced damage in Ge: strain and disorder profiles during defect accumulation and recovery. *J. Phys. D: Appl. Phys.* 42, 165404, doi: 10.1088/0022-3727/42/16/165404 (2009).
- 24 Claverie, A., Koffel, S., Cherkashin, N., Benassayag, G. & Scheiblin, P. Amorphization, recrystallization and end of range defects in germanium. *Thin Solid Films* 518, 2307-2313, doi:10.1016/j.tsf.2009.09.162 (2010).
- 25 Yeh, M. S., Lee, Y. J., Hung, M. F., Liu, K. C. & Wu, Y. C. High-Performance Gate-All-Around Poly-Si Thin-Film Transistors by Microwave Annealing With NH₃ Plasma Passivation. *IEEE Trans. Nanotechnol.* 12, 636-640, doi:10.1109/tnano.2013.2265778 (2013).

Chapter 4

Epitaxial post-implant recrystallization
in germanium nanowires

4.1. Abstract

As transistor dimensions continue to diminish, techniques for their fabrication need to be adapted. In particular, crystal recovery post ion implantation is required due to destructive ion bombardment inducing crystal damage including amorphisation. In this chapter, we report a study on the post-implant recrystallization in Ge nanowires (NWs) following gallium (Ga) ion doping. In this work a variation of NW diameters and orientations were irradiated and annealed in situ to investigate the mechanism of recrystallization. An added complication of misorientation of crystal grains increases the complexity of crystal recovery for suspended NWs. We show that when the misorientation is prevented, by leaving a crystal link between two seeds and providing a rigid support, recrystallization occurs primarily via solid phase epitaxial growth (SPEG). Finally, we demonstrate that top-down fabricated Ge NWs on insulator can be recovered with no extended defects. This work highlights both experimentally and through molecular dynamic simulations the importance of engineering crystal recovery in Ge NWs which may have potential for next-generation complementary metal-oxide semiconductor (CMOS) devices.

4.2. Introduction

Accurate control of doping is vital when fabricating NW FETs^{1, 2} and other NW devices such as sensors,^{3,4} photovoltaics⁵ and photonic devices.⁶ In inversion mode nanowire FET devices, variability issues are attributed to non-uniform dopant distribution.⁷ There has been a lot of research on the control of dopant depth as well as concentration which has seen the development of new doping techniques such as

Chapter 4. Epitaxial post-implant recrystallization in germanium nanowires

molecular layer doping and single ion doping.⁸⁻¹¹ Ion beam doping is currently common practice in industrial microprocessing, but transferring this technique to nanostructures is challenging. For ion beam doping the dopant atom (and resulting cascade recoils) can be easily lost/ejected if the path of the dopant atom leaves the nanowire volume and hence the energy of the ion beam needs to be selected depending on the desired depth of implantation. Moreover, the destructive nature of ion beam doping due to ion bombardment and resultant cascade recoils within the NW volume requires a crystal recovery step.¹² An increase in conductivity has been demonstrated in grown Ge NWs irradiated with a Ga ion source up to a fluence of $6.25 \times 10^{12} \text{ cm}^{-2}$ without an activation (annealing) step.¹³ Above this fluence, a drop in conductivity is observed and is attributed to amorphisation. However, higher implantation fluences are required to achieve the proper function of advanced transistors such as junctionless nanowire transistors (JNTs)¹⁴ and photonic devices.¹⁵⁻¹⁶ Unfortunately, full recovery of irradiated nanostructures is not easily achievable.^{12, 17}

Thermal annealing is the final step required to activate the implanted dopant atoms and recover the crystallinity of the nanowire. Recrystallization occurs via two competing mechanisms; solid phase epitaxial regrowth (SPER) and random nucleation and growth (RNG).²⁵ It has been observed, like silicon, the germanium [111] direction is the least favourable for crystallization and {111} stacking faults are common.²⁹⁻³⁰ It has been predicted by molecular dynamics simulations that the recrystallization process in nanowires can be largely influenced by the presence of interfaces which propagate the formation of stacking fault defects.³¹ Simulations of

Chapter 4. Epitaxial post-implant recrystallization in germanium nanowires

the defect dynamics have also shown that such defects are pinned at the nanowire surface and can be a result of overlapping growth fronts.

There has been an extensive body of research investigating the recrystallization of bulk Ge and some progress in recent years on Si and Ge nanostructure recrystallization post ion irradiation.^{12, 17-22} The high surface-area to volume ratio in nanostructures results in a greater sensitivity to surface roughness and possible over-layers.^{23,24} Therefore, formation of dangling bonds, and by extension stacking faults, are prevalent during regrowth.^{12, 17} The bulk material acts as a seed for the recrystallization of fin structures and nanopillars via SPEG, however, a polycrystalline region is observed to occur at the top of the structure (i.e. not in proximity to the bulk crystal seed).^{20, 25} This polycrystalline region is likely due to the predominance of RNG. NWs with no contact to a bulk substrate which undergo ion irradiation along its entire length, and hence experience full amorphisation, lack the seed which facilitates SPEG and hence recrystallization occurs solely via RNG. However, recrystallization of Ge fin structures has been shown to achieve full recrystallization via SPEG with high defect density at the top of the structures.¹⁷ Another undesirable factor which affects the recrystallization of NWs is loss of rigidity (bending) with ion bombardment induced amorphisation. A misorientation between two crystalline fronts results in a crystal mismatch and hence defect formation.²⁶ It has been shown that NWs can be bent in a desired direction depending on the energy and the direction of the incoming ion beam.^{21, 27-28} Bending occurs to minimize stress within the NW due to amorphisation. The stress may be due to formation of a crystalline/amorphous (c/a) interface,²¹ a combination of

Chapter 4. Epitaxial post-implant recrystallization in germanium nanowires

compressive and tensile stress due to formation of vacancies and interstitials,²⁸ or it may be due to densification during irradiation.²⁷ Importantly, the influence of the topology of the c/a interface and the rigidity (bending) of the NW on high temperature regrowth has not been investigated.

An understanding of the recrystallization process will aid in the engineering of defect-free highly doped nanostructures. Experimental data coupled with modeling calculations have already shown the dependence of crystal orientation for the rate of recrystallization.^{17,32-34} In this work, a detailed investigation into Ge NW recrystallization post Ga-ion irradiation by in situ TEM combined with molecular dynamics calculations is presented. The main aim of this study is to devise a method to reduce residual defects after recrystallization in Ge NWs. By minimizing the contribution of RNG and the role of misorientation in the recrystallization fronts due to NW bending, a predominately SPEG mechanism and defect-free regrowth is promoted. It is demonstrated that NW partial amorphisation allows for single crystal seed remnants which facilitate SPEG recrystallization as growth templates. For the investigation of the role of misorientation of crystal seeds for regrowth, NWs were encapsulated in an external amorphous matrix on a flat wafer support to preserve their rigidity during irradiation. Combining these approaches, post-anneal Ga-ion implanted Ge NWs (with implantation doses up to $4.8 \times 10^{15} \text{ cm}^{-2}$) with no apparent stacking fault defects were demonstrated on buried oxide.

4.3. Experimental Procedure

4.3.1. Concurrent imaging platform and irradiation

The method for platform preparation, concurrent imaging and doping of NWs using a dual beam FIB/SEM, has been described previously in Chapter 2 section 2.3.3.¹² For accurate selective area doping within a section of single NW it is important to align the electron and ion beam coincident point precisely as the exposure needs to be done “blind” with the aid of the electron beam for navigation. A 30 keV Ga ion beam, operating at a current of 9.6 pA, was used for all implantation experiments presented here. A rectangle area is defined for the irradiations. The length of the NWs irradiated varied between 200 nm and 1 μm . The typical area irradiated was 200 nm (along length of NW) \times 5 μm . A minimum dose of 1.9×10^{13} ions cm^{-2} was used in the experiments presented here. Small areas can be accurately irradiated with Ga ions without introducing impurities to the surrounding structures by using a well-aligned FIB.

4.3.2. Irradiated EBL defined GeOI Nanowires

An overview of the experimental procedure for the irradiation and imaging of NWs is depicted in a schematic in Figure 4.1. NWs deposited on silicon nitride (SiN) membranes do not require any additional steps for observing the damage incurred and subsequent in situ TEM annealing (Figure 4.1 a).¹² For the NWs on a substrate, grown NWs deposited on a Si/SiO₂ chip via dry transfer from the growth substrate or EBL defined NWs on GeOI (germanium on insulator) were used.³⁵⁻³⁶ In order to observe the in situ TEM recrystallization along the NWs on substrates, the structures need to be extracted with the underlying substrate

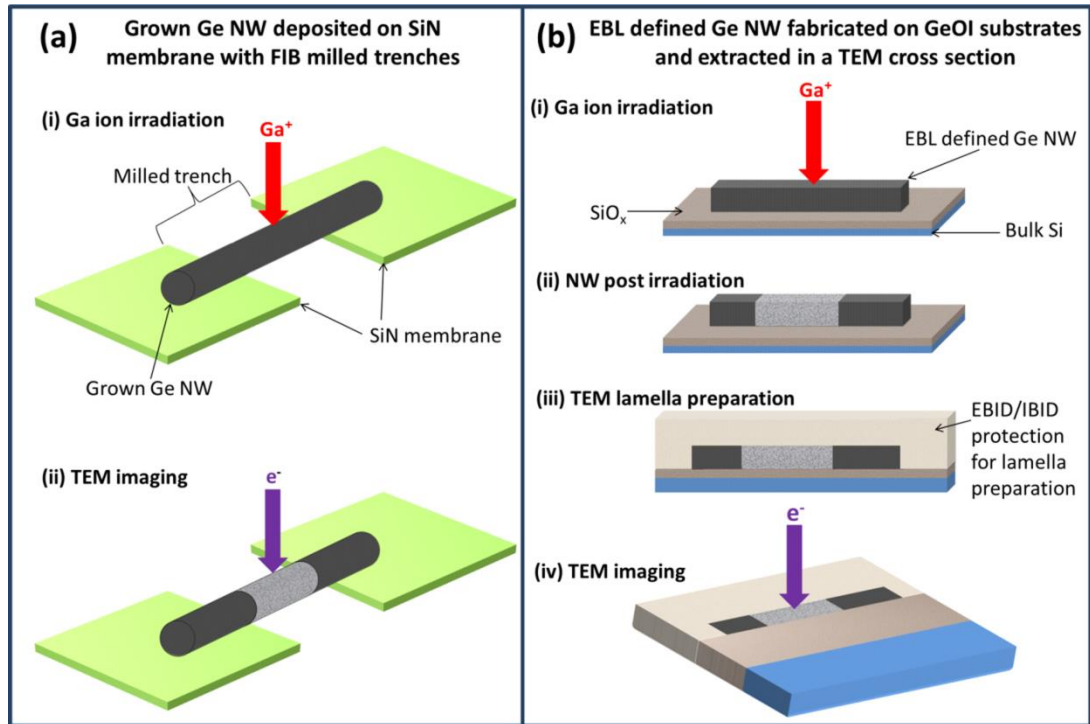


Figure 4.1. Schematic overview of sample preparation and imaging for (a) a nanowire on pre-patterned SiN membrane and (b) EBL defined NW from on GeOI substrate.

(Figure 4.1 b iii). This is done via a non-typical inline FIB lift-out technique along the NW length (Figure 4.2). For all NWs imaged on SiN membranes, the direction of the ion beam (red arrow) during irradiation is nearly parallel to the electron beam (purple arrow) when imaged in the TEM (Figure 4.1 a). However, for NWs extracted from a substrate (Figure 4.1 b) the direction of the ion beam is orthogonal to the direction of the electron beam when imaged in the TEM, i.e. we have a side view of the irradiated NW along its length. The GeOI NWs defined by EBL have a height of approximately 50 nm, which is almost twice the range of interactions of the 30 kV Ga-ions in Ge. Therefore, to achieve amorphisation across the NW (the width of the NWs is approximately 40 nm) and avoid ion channeling, very high ion-beam incidence angles ($\pm 62^\circ$) were used (Figure 4.3).

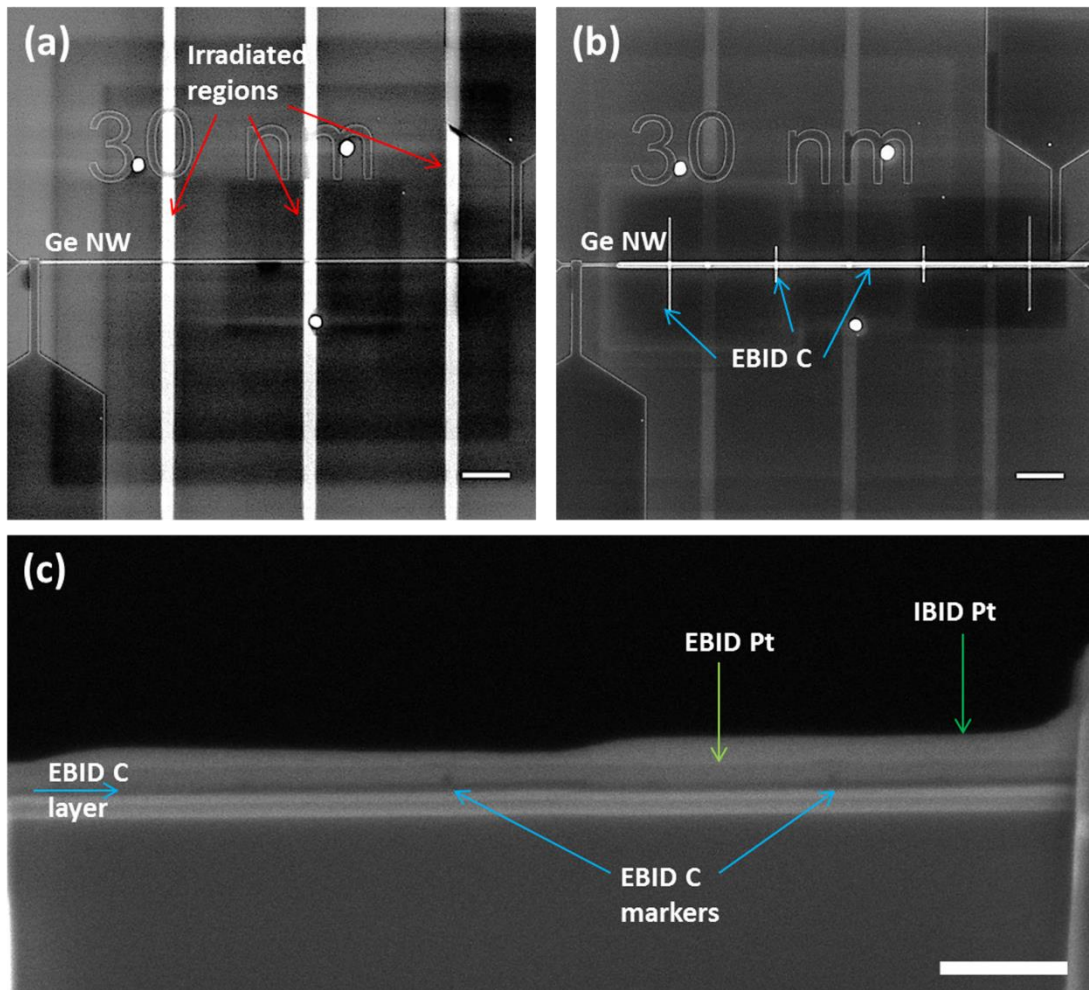


Figure 4.2. Overview of use of EBID carbon for indication of NW exposure during thinning. Scale bar for all images is 1 μm .

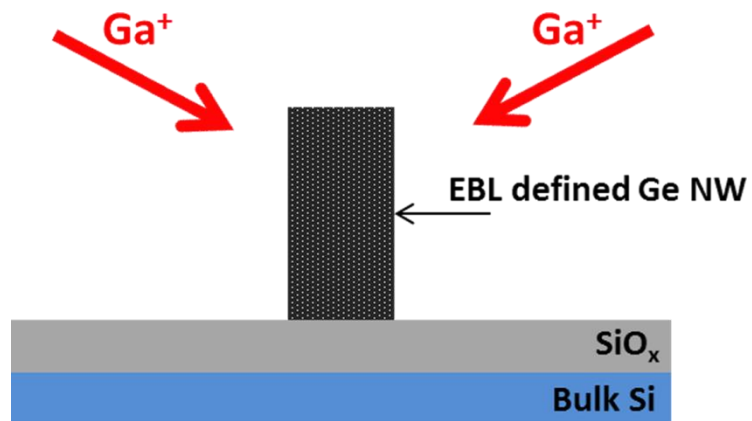


Figure 4.3. Schematic of 62° tilt ion irradiation of EBL defined Ge NW in cross sectional view.

4.3.3. In situ anneal

An in situ Gatan Model 628 single-tilt heating stage TEM holder was used for all anneals presented in this study. The ramp/temperature used for each NW varied. The sample was loaded in the same orientation in the in situ heating stage as it was for HRTEM imaging in the double tilt holder. The in situ heating stage is only capable of single tilt so the sample was tilted as close to the zone axis used for high resolution imaging as possible. For most samples tilting in two directions is required to achieve a zone axis orientation for lattice resolution imaging. The TEM was operated in bright field mode, isolating the direct beam with the objective aperture, to take advantage of the contrast between the crystalline and amorphous regions. Temperature was controlled using a Gatan Model 901 SmartSet hot stage controller. Temperatures varied from 100 – 500 °C (the temperature dispersion control is approximately 0.1 - 0.5 °C, as per the manufacturer's specifications). Images were acquired every minute at the set temperatures.

4.4. Results and Discussion

4.4.1. Recrystallization of nanowire with extensive amorphisation

In order to examine Ge nanowire crystal recovery, the same nanowire from Figure 3.6 was thermally annealed in situ in the TEM at 490 °C. For the initial 20 min of the anneal there is no apparent crystal growth; this could be due to the resolution of our technique. There is likely curing of crystal fronts in the first 20 min. The remaining crystalline islands, identified as the dark regions in Figure 4.4 are approx. 10 nm in

diameter and located, at the back and middle of the nanowire with respect to the direction of the incoming beam as discussed before. These crystallites are the only remaining “seed” available for the crystal regrowth.⁴¹

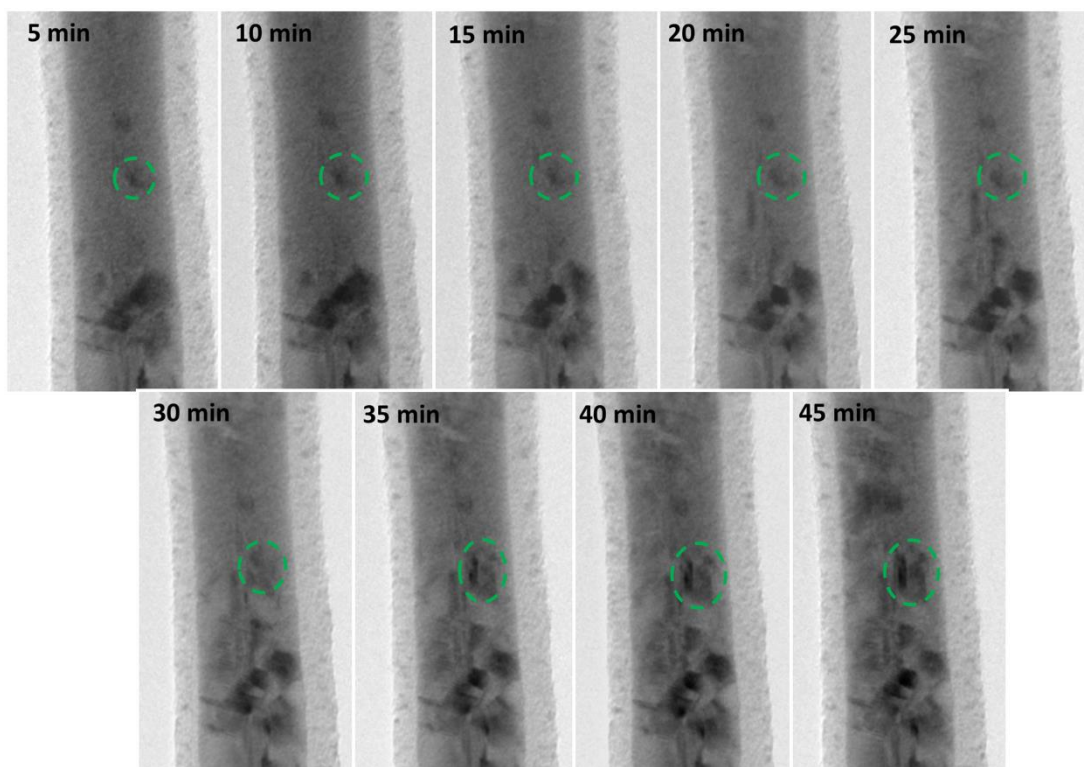


Figure 4.4. In situ anneal of nanowire after implantation at 490 °C for 45 min. There is a large amorphous layer around the NW which is a build-up of contamination (carbon). Green circle highlights an example of a crystallite growth during the anneal.

As seen from the sequence of images in Figure 4.4, the crystallites grow in size after developing recrystallization fronts in the surrounding amorphous region an example is highlighted (green circles) in Figure 4.4. Self-nucleation of crystallites in the amorphous regions can also not be excluded. The final image in Figure 4.4 shows the nanowire after 45 min at 490 °C with corresponding lattice resolution images in Figure 4.5. The crystallisation process resulted in a complex mixture of a large number of extended defects; mainly (111) stacking faults including the recovery of

Chapter 4. Epitaxial post-implant recrystallization in germanium nanowires

the stacking fault sequence that existed before the irradiation (see Figure 3.6 (a) for comparison). Although, the majority of the newly formed (111) stacking faults were pinned to the nanowire surface (shown with black arrows), some are parallel to the side wall facets and the initial stacking fault sequence (shown with white arrows). At the regions where these defects overlap a complex pattern is formed (marked with dashed boxes), that can be understood as interference patterns due to overlapping twinned grains.⁴²

Interestingly, the majority of the newly formed (111) stacking faults formed an ordered arrangement, similar to stacking faults identified in grown nanowires previously.^{29, 43} The crystallisation nucleated from separate crystal islands. The growth results in epitaxial recovery until recrystallization fronts meet, forming a planar defect. Obtained recrystallization data collaborate very well with the molecular dynamics simulations obtained for Si nanowires.³¹ The appearance of newly formed defects and recovery of the parent crystal can be attributed to two separate processes: (i) epitaxial propagation of recrystallization fronts (fastest growing in the (110) and (100) directions, as predicted previously³⁸) and (ii) the interaction of these fronts when self-intersected and with the nanowire surface. These two processes result in formation of (111) stacking fault defects as well as epitaxial recovery of the rest of the nanowire including pre-existing defects. The fact that the majority of the newly formed stacking faults are pinned to the nanowire surface suggests that the surface plays a predominant role in defect formation.

Significantly, using developed correlative analysis platform, detailed recrystallization data (Figure 4.4) were recorded in the same region of the nanowire

that has been ion-beam damaged (Figure 3.6); hence allowing a direct correlation of structural transformations as result of ion beam damage and thermal annealing.

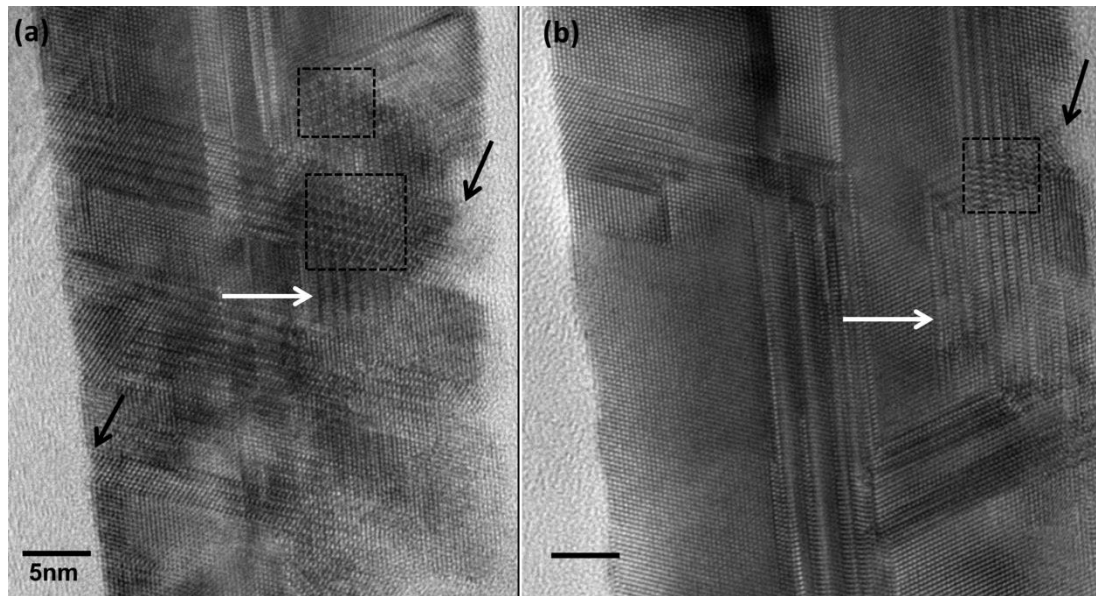


Figure 4.5. Lattice resolution images of nanowire post recrystallization at (a) region of interest showing a high density of stacking fault defects as well as an increase in edge roughness. In another region of the same nanowire (b) a mixture of intrinsic defect curing, high density defect formation and retention of original crystal structure are all observed. Scale bar for image is 5 nm.

4.4.2. Recrystallization of nanowire with partial amorphisation

Another nanowire was irradiated within a selected region to induce amorphisation only within the selected section. Figure 4.6 (a) and (b) show TEM images of a 38 nm diameter $\langle 111 \rangle$ grown NW (NW1), imaged along the $[\bar{2}11]$ zone axis, irradiated to induce full amorphisation in a 200 nm section of the NW length. Note that the NW is suspended across an open trench of the SiN membrane. A misorientation is observed between the two crystalline regions, X and Y, separated by the amorphous region which is approximately 205 nm in length. The two crystalline regions were estimated to be at a relative angle (θ) of approximately 3° to each other.⁴⁴ Although only a

Chapter 4. Epitaxial post-implant recrystallization in germanium nanowires

small region experienced full amorphisation, damage to the NW (partial amorphisation) is observed extending approximately 300 nm either side of the region which was irradiated.

In situ annealing of the NW was observed in the TEM at 400 °C for 83 min and subsequently at 450 °C for 37 min (Figure 4.6 d). An amorphous layer is observed to develop around the NW during the anneal; this is commonly observed during in situ TEM annealing experiments and it is due to carbon-based contaminants desorbed at high temperatures and redeposited due to EBID. Because there was a misorientation of the two crystal seeds only one seed was selected for observation during the anneal process. Within the first 25 min of the anneal, the damaged region, which experienced partial amorphisation and contains many crystallites, developed a continuous crystal growth front (Figure 4.6 (d) at 25 min). The recrystallization appears to occur preferentially along the length and in the center of the NW forming an arrow-head type crystal front. As the crystal front approaches a fully amorphous region, the crystal front flattens, which is expected as growth in the $\langle 111 \rangle$ direction is least favorable.⁴⁵ The arrow-head recrystallization front is observed again when the temperature is increased to 450 °C (and the rate in turn increases) until a point when the front meets region Z. The recrystallization rate was estimated by measuring the crystalline region from the images acquired during the anneal. See Figure 4.A in the appendix for the analytical procedure adopted to determine crystal regrowth rates with the TEM images acquired during the anneal.

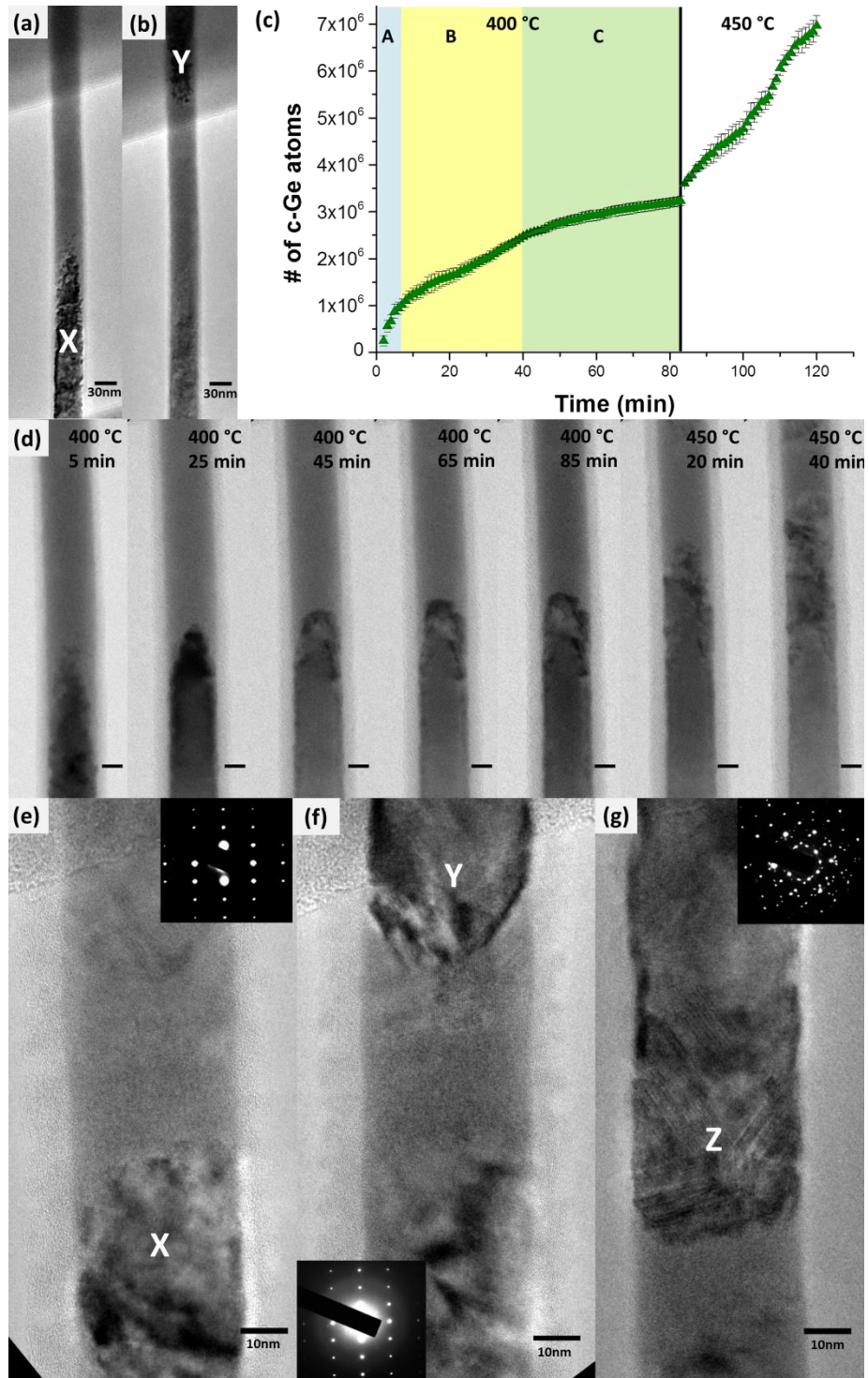


Figure 4.6. NW after irradiation to only part of the length which experiences full amorphisation, (a) and (b). (c) Graphical representation of recrystallization. (d) Selected images from the in situ anneal at 400 °C for 83 min and a further 37 min at 450 °C. Focus issues encountered due to thickness variations and thick carbon layer which developed around NW. Scale bar is 5nm. Before the anneal (a, b) regions X and Y are approximately 3° relative to each other. After the anneal (e-g) regions X and Y maintain the misorientation with a relative angle of 4.2° and the third region Z is at a relative angle of 17° and 14.7° to X and Y, respectively.

A graphical representation of the calculation results is presented in Figure 4.6 (c). The measurements were completed at least three times to achieve a statistically correct overview. It can be observed that a constant rate is not observed for the duration of the 400 °C anneal. The initial recrystallization rate for the first 5 min was approximately 3405 atoms s⁻¹ (Figure 4.6 (c) region A), which decreased to 700 atoms s⁻¹ for minutes 6-40 (region B) after which the rate dropped again to 280 atoms s⁻¹ (region C). The recrystallization rate after the temperature increase to 450 °C rose again to 1600 atoms s⁻¹. The initial high recrystallization rate is postulated to be due to the higher number of mono-oriented and connected crystalline seeds within the partially damaged region which act as preferential growth sites.⁴⁶ Similar deviation from linear growth has been observed previously for Ge and particularly for short anneal times for thin amorphous layers and has been attributed to void formation or the introduction of oxygen during the anneal.⁴⁵ In another study, it was shown that the rate of SPEG decreased as the growth front approached within 0.3 μm of the surface and has been attributed to H infiltration and this has a higher impact on Ge than Si SPEG.⁴⁷

Figure 4.6 (e), (f) and (g) show HRTEM images of the recrystallized NW after annealing. The mismatch of the two crystal planes was retained with the formation of a highly defective region between the two crystal grains, region Z. The relative angles for the crystal grains imaged were calculated; $\theta_{XY} = 4.2^\circ$; $\theta_{YZ} = 17^\circ$; $\theta_{XZ} = 14.7^\circ$. The region between grains X and Y appears to be amorphous but when imaged in the zone axis for Z it is clear that it is in fact crystalline. The formation of the defective grain (Z) is highly irregular. The smallest possible angle between

$\langle 211 \rangle$ and $\langle 011 \rangle$ is 30° . The two original grains, X and Y, are both in the $[\bar{2}11]$ zone axis and C is in the $[011]$ zone axis. The relative angle between $\langle 211 \rangle$ and $\langle 011 \rangle$ directions were calculated from

$$\cos \theta = \frac{(hH+kK+lL)}{\sqrt{(H^2+K^2+L^2)(h^2+k^2+l^2)}}$$

where the two axes are (hkl) and (HKL). A plausible explanation for this unexpected grain formation is RNG in the strained region. Regions X and Y have maintained the original crystallographic relationship with a misorientation between the two regions. However, region Z has no rational crystallographic relationship with either regions X or Y indicating a polycrystalline growth due to RNG. It has been shown that a NW can be bent in a desired direction upon FIB exposure and maintains the bent shape even after high temperature annealing.^{21, 27-28} The result for NW1 correlates well with results on Si NW recrystallization published by Pecora et al. in which NWs were irradiated and experienced bending.²¹ Some NWs, presented by Pecora et al., straightened during recrystallization and were single crystalline, albeit partially defective, but NWs which remain bent were polycrystalline. Summarizing the mechanism of recrystallization for the suspended Ge NW (Figure 4.6) two different regrowth mechanisms can be identified (single crystalline vs polycrystalline) with SPEG resulting in the single crystalline regrowth from regions X and Y, and RNG resulting in the polycrystalline regrowth in region Z.

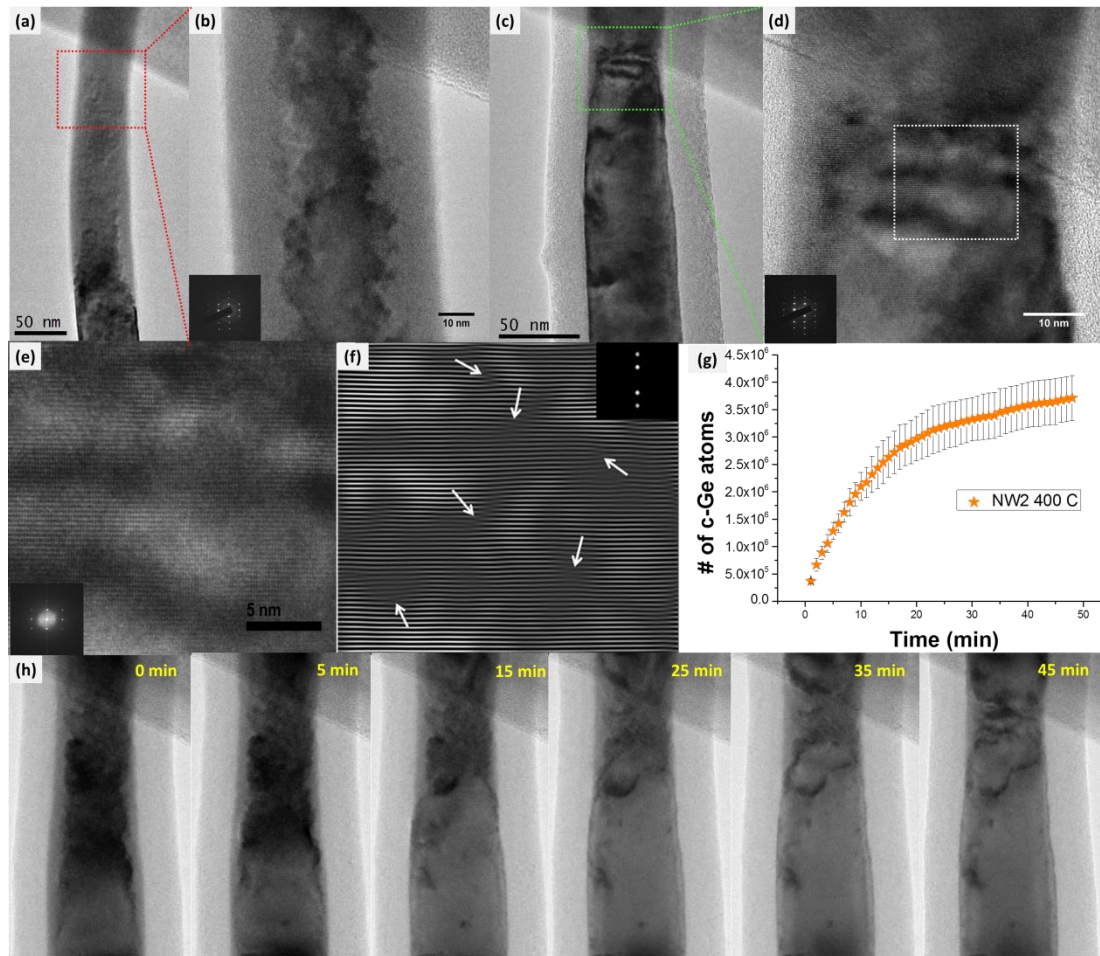


Figure 4.7. NW2 (a) and (b) partially irradiated with remaining crystal in irradiated region imaged along the $[\bar{2}11]$ zone axis. (c) and (d) after annealing at 400 °C for 47 min. (e) A high resolution lattice image of region identified in (d). (f) Inverse of $\langle 111 \rangle$ reflections from FFT of (e). White arrows indicate misfit dislocations. (g) Graphical representation of recrystallization. (h) Selected images from the in situ anneal at 400 °C for 47 min.

A (larger) 56 nm diameter $\langle 111 \rangle$ grown NW also imaged in $[11\bar{2}]$ zone axis was irradiated to induce amorphisation but retain a crystalline “backbone” for a section of the NW across an open trench of a SiN membrane (Figure 4.7) . A cross section of another irradiated 50 nm $\langle 111 \rangle$ grown NW has been presented in Figure 3.5 (c). Depending on the energy of the ion beam, the range of the ions can be estimated.⁴⁸ In this case, a 30kV Ga ion beam does not have enough energy to penetrate and induce cascade recoils through the whole diameter of the NW and hence a crystal region

remains along the back of the NW. This backbone provides a support for the NW, maintaining some rigidity by preventing misorientation and allowing a direct link between the two non-irradiated regions. It is observed in Figure 4.7 (a) that the NW experiences some bending. The only way to avoid this bending for a grown NW is to provide a flat and stable support, e.g. on Si_3N_4 or SiO_2 substrate as we show below. The thermal anneal of NW2 was observed in situ in the TEM at 400 °C for 47 min (Figure 4.7 h). An estimation of the recrystallization rate is represented graphically in Figure 4.7 (g). When recrystallization occurred in the NW1 in Figure 4.6 there was a clear interface between the crystalline and amorphous regions. In Figure 4.7 (a) and (b), the volume of the amorphous region is difficult to quantify based on the images alone. Thus, the estimation of the recrystallization rate calculated for NW2 is an underestimation of the rate and volume of Ge recrystallized. The initial recrystallization rate for the first 15 min is estimated to be $3130 \text{ atoms s}^{-1}$. HRTEM images post-anneal show a monocrystalline NW (Figure 4.7 c-e). No stacking fault defects are observed along the growth direction of the NW imaged in the $[11\bar{2}]$ zone axis. From the reconstructed FFT (Figure 4.7 f), the presence of dislocations in the crystal can be identified (white arrows), these are likely to be stacking faults along the $(\bar{1}11)$, $(1\bar{1}1)$ and/or $(11\bar{1})$ planes. To confirm these “hidden defects” it would be required to tilt to another zone axis such as the $[011]$ zone axis.⁴⁹

In an attempt to reduce and understand the influence of strain experienced by a suspended NW, a NW deposited on a substrate was irradiated, encapsulated and recrystallized in situ (Figure 4.8) (NW3). The 64 nm diameter, $\langle 112 \rangle$ grown NW containing intrinsic $(11\bar{1})$ stacking faults along the NW length was imaged along the

[1 $\bar{1}$ 0] zone axis. NW3 was irradiated on a Si/SiO₂ substrate and then extracted as an inline FIB cross-section, i.e. along its length (Figure 4.2). In this method, the NW is encapsulated in EBID carbon. A section approximately 500 nm along the NW was defined for irradiation but a length of approximately 600 nm experienced amorphisation (Figure 4.8). As observed in Figure 4.8 (a), only partial amorphisation across the NW diameter is achieved leaving a continuous backbone similarly to the NW2. The embedded NW was annealed in situ at 400 °C for 30 min (Figure 4.8 g). It is clear from the images taken in situ that the recrystallization occurs epitaxially, i.e. via a SPEG mechanism. Two major crystal fronts can be identified; one in the [11 $\bar{1}$] direction orthogonal to the NW long axis, which is the larger growth front, and the other growth front in [112] direction, i.e. the NW growth direction. HRTEM images post-anneal show a mixture of defect curing, intrinsic defect propagation as well as the appearance of newly formed (extrinsic) defects (Figure 4.8 e). Some of the extrinsic defects formed are ($\bar{1}$ 11) stacking faults in the same direction as the intrinsic defects (along the NW length) and the rest are {111} stacking faults which are pinned to the NW surface. Interestingly, the region towards the middle of the amorphous area recrystallized with the formation of mainly extrinsic stacking faults. The intrinsic defect propagation is limited to the edges of the damaged region. The recovery of intrinsic stacking faults from a fully amorphous structure, i.e. the phenomenon of crystal memory, an apparent memory of an amorphised material which retains some ordering and hence fully retains the crystal structure upon recrystallization without the assistance of an epitaxial template, has not been observed.

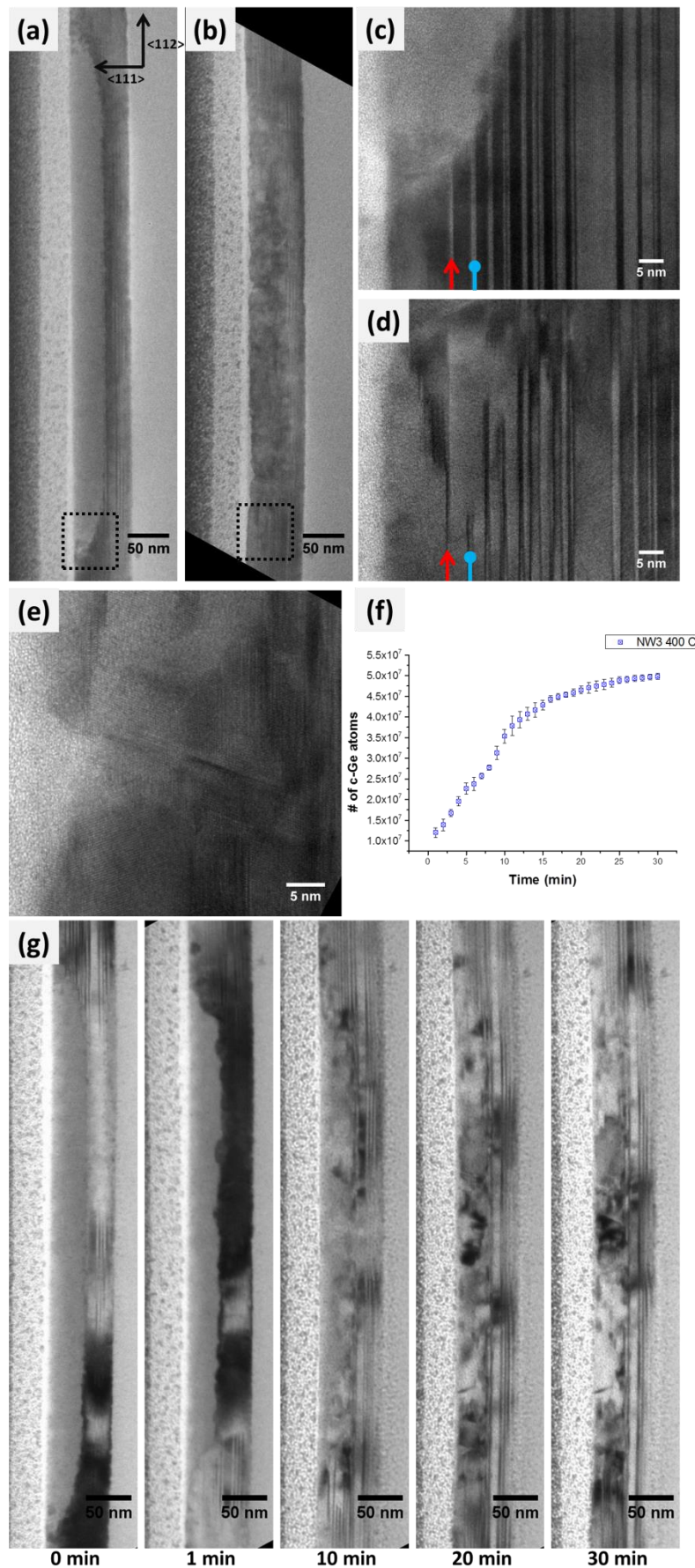


Figure 4.8. $\langle 112 \rangle$ grown NW3 (a) after irradiation and (b) after anneal at 400 °C for 30 min. (c) and (d) are higher resolution images from the marked regions in (a) and (b) respectively. The red arrow indicates SF1 and the blue pin indicates SF2. (e) HRTEM of recrystallized NW3 from middle of damaged region post-anneal. A combination of $\{111\}$ stacking faults pinned to the surface, stacking faults parallel to intrinsic defects and defect free regions are observed. (f) Graphical representation of Ge recrystallization rate during the anneal of NW3. (g) Selected images from the in situ anneal of NW3 at 400 °C for 30 min. Changes in contrast of the NW are observed during the anneal due to drift moving the sample further away from the zone axis.

However, seeding of parallel stacking faults through defects in the Au seed and their propagation along the $\langle 112 \rangle$ grown Ge NWs has been reported.²⁹ For stacking fault 1 (SF1) (indicated with red arrows in Figure 4.8 c), there is a damaged region which has not experienced full amorphisation, this is due to cascade recoils being ejected from the NW volume.^{12, 19} A broadening is observed for SF1 grain in Figure 4.8 (d) post-anneal. This type of migration has been previously observed where it was attributed to the slower growth rate in $\langle 111 \rangle$ than in the $\langle 115 \rangle$ direction, resulting in a migration of the twin grain in a stepwise fashion.⁵⁰ At stacking fault 2 (SF2) (indicated with blue pins in Figure 4.8) the c/a interface is sharp with little or no ordering present. The bulk crystal grain engulfs the stacking fault and effectively prevents propagation of the stacking fault in the $\langle 112 \rangle$ direction. This illustrates the importance of the roughness of the c/a interface. An initial recrystallization rate of $39046 \text{ atoms s}^{-1}$ was estimated for the first 15 min based on the images from the in situ anneal. As observed for the previous two anneals, the rate begins to level off as the NW recrystallizes fully.

A Ge NW (NW4) was defined via EBL from a (001) GeOI wafer along the [100] direction. The etched NW4 with rectangular cross-section (width 40 nm, height 55 nm) was irradiated and annealed in situ, imaged close to the [010] zone axis (Figure 4.9). The irradiation was done at high incidence angles ($\pm 62^\circ$, i.e. -10° tilt of the stage) to induce amorphisation as the width of the NW is less than the height of the Ge (Figure 4.3). Annealing was initiated at 100°C with incremental increases in

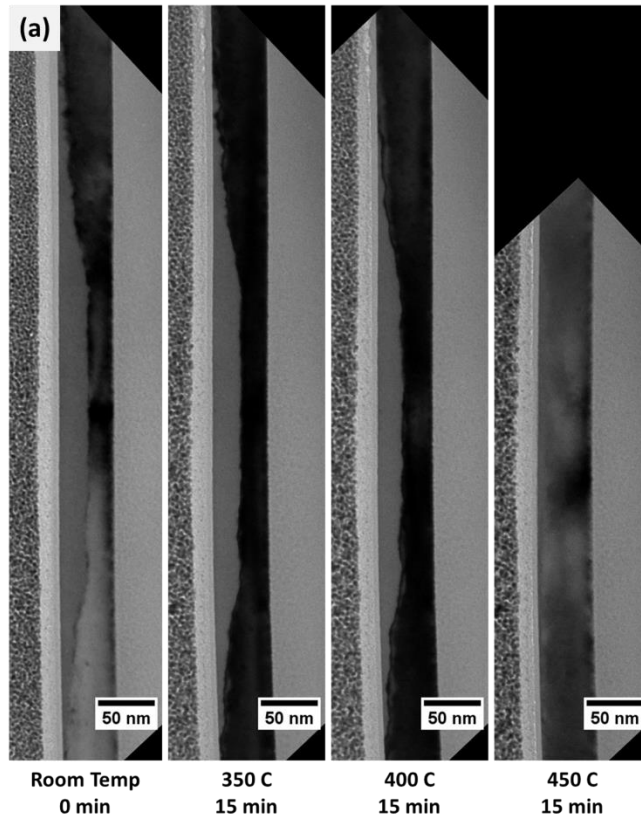
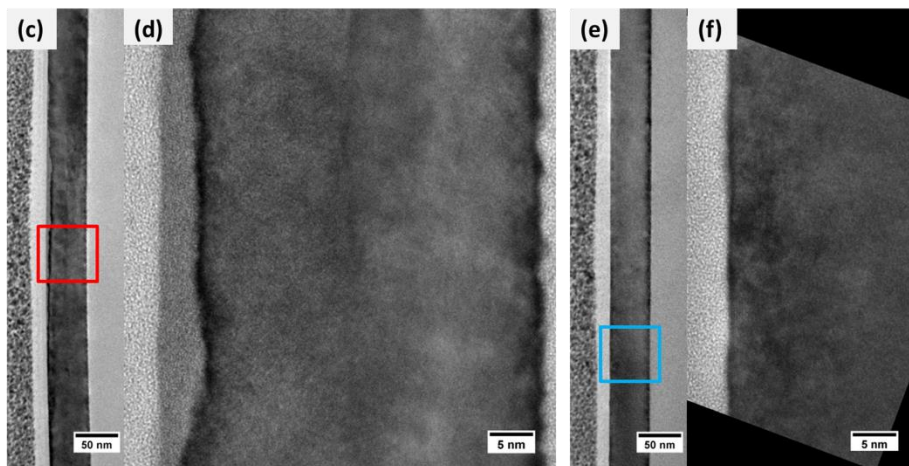
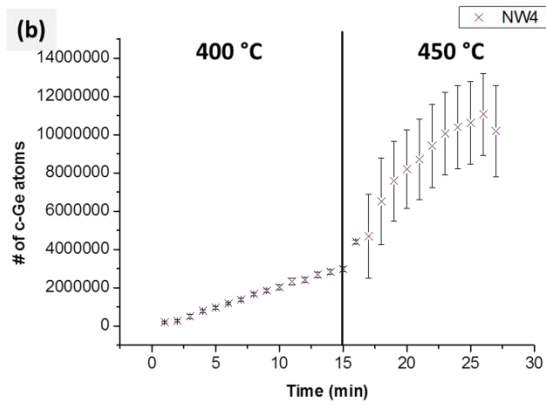


Figure 4.9. (a) In situ anneal of Ge[100] NW (NW4). The NW was heated incrementally from 100 °C to 450 °C in 50 °C increments and remaining at each temperature for 15 min. (b) Graphical representation of recrystallization of NW4 at 400 °C and 450 °C. (c) and (d) NW4 after the in situ anneal. (e) and (f) After further anneal with a rapid ramp directly to 400 °C and then to 500 °C for 10 min.



steps of 50 °C every 15 min. Notable recrystallization was only observed from 400 °C. Recrystallization rates were extracted from the in situ images for 400 and 450 °C, approximately 3480 and 18570 atoms s⁻¹, respectively (Figure 4.9). The initial heating rate affects the recrystallization temperature observed.⁵¹ Estimation of the recrystallized volume is more accurate as the cross sectional shape of GeOI NW is rectangular. Similar to NW3, two recrystallization fronts can be identified; predominantly along the [001] direction. A final anneal with a direct ramp to 400 °C followed by a temperature increase 500 °C was done to fully recover the crystallinity of the NW. Based on the HRTEM images acquired, in Figure 4.9 (f), no stacking fault defects were observed and this is attributed to the SPEG.

Activation energies (E_a) in the range between 2.0 eV and 2.19 eV have been previously reported for Ge recrystallization.^{45,52-55} To calculate the E_a of recrystallization in a NW, the rate of recrystallization of two different temperatures for the same NW were used, the calculation is described in the Supporting Information. For this report, NW4 was used to calculate a crude estimation of the E_a of recrystallization to be approximately 1.4 eV. Only this NW was used for the E_a calculation due to the slow ramp rate for both temperatures (400 and 450 °C) for the calculation and the abundant amorphous “sink” for both anneal temperatures, i.e. less than 50% of the volume recrystallized at the 400 °C. The contribution of the electron beam was not accounted for in the calculations of activation energy. The anneal of NW4 was initiated at 100 °C with recrystallization only observed from 400 °C. This would suggest that the electron beam had little or no effect on the recrystallization. However the oriented attachment of crystals and further extended growth from

Chapter 4. Epitaxial post-implant recrystallization in germanium nanowires

amorphous phase has been observed in systems such as suspensions of NPs⁵⁶ and by us in ALD (atomic layer deposition) deposited hafnia films (unpublished results). The temperature distribution in an electron transparent metal sample has been measured by EELS to obtain nanoscale maps of the temperature distribution when metal circuits are electrically loaded.⁵⁷ This is done by looking into changes in the plasmon band at different temperatures along the metal lines. Possibly this can be extended to calculating the activation energy of various thermally associated reactions at the nanoscale. The E_a obtained in MD simulations was 0.92 eV which confirms a slightly smaller value in comparison to simulations of planar recrystallization, where the activation energy was $E_a=1.09$ eV.³⁸

A notable difference between irradiated NWs and bulk substrates is the shape of the c/a interface. In a bulk substrate, the c/a interface may be rough but the interface is relatively flat so recrystallization occurs primarily in one direction. For a grown NW with a remaining crystal backbone the interface has two extra dimensions to consider – the crystal fronts created at the edge of the irradiated region and the curved cross sectional interface. Although the crystal backbone has proven successful in facilitating SPEG any strain may result in misorientation, as seen in the suspended NWs, and hence defect formation. With an increase in rigidity, i.e. presence of crystal seed (backbone), and a rectangular cross section the post-implantation anneal of the top-down fabricated NW4 is more comparable with a bulk substrate, resulting in almost defect-free SPEG. From a device perspective, patterned Ge NWs developed by lithography (not necessary EBL) show greater promise for large-scale device fabrication in comparison to grown structures.⁵⁸

4.5 Conclusions

Suspended Ge NWs that have experienced full amorphisation after irradiation and have lost their rigidity (i.e. bent NWs after irradiation), although having crystal seed templates, show competing action of the SPEG and RNG processes, resulting in highly defective and poly-crystal growth. A loss of ordering with amorphisation results in misorientation of crystal seeds in NWs due to deformation with decreasing rigidity. The effect of misorientation of the crystal grains due to ion beam induced bending is minimized when the amorphisation is limited to allow a crystalline backbone and/or with external support in a matrix. The minimized misorientation resulted in diminished RNG and hence SPEG was promoted.

Recrystallization of a NW is complex due to the high surface area and hence sensitivity to any alteration to the surface, such as surface roughness and H infiltration.⁴⁷ {111} stacking fault pinning at the surface of the NW has been directly observed in this study. This result highlights the contributing factor that the surface-area to volume ratio has on NW recrystallization for both the rate and crystal structure.

It has been observed that for $\langle 111 \rangle$ grown NWs, no defects formed in the growth direction of the NW, i.e. no lateral (111) stacking faults are formed.³⁰ However, for the $\langle 112 \rangle$ grown NW containing intrinsic $(\bar{1}11)$ longitudinal defects, extrinsic $(\bar{1}11)$ defects parallel to the intrinsic defects formed as well as {111} stacking fault defects pinned to the surface. In other studies, a high temperature anneal has shown to cure extrinsic {111} stacking faults¹⁷ but a thermal budget for device fabrication may limit process temperatures. An alternative potential route for ion beam doping of

nanostructures is moderate heating (approximately 250 °C) during irradiation which promotes dynamic annealing.⁵⁹

In summary, crystal recovery of grown and top-down fabricated Ge NWs studied using in situ TEM has been presented. Using in situ TEM data supported by MD calculations, we demonstrate that the recrystallization of the Ge NWs is complex and may result in structures having polycrystalline regions, large number of extended crystal defects such as stacking faults, and in some cases full crystal recovery. We identified that factors such as the amount of initial crystal damage and associated rigidity of the NWs as well as the roughness of the c/a interface and the surface to volume ratio, i.e. proximity of the re-growth front(s) to the surface are very important in engineering the NW crystal recovery.

4.6 References

- 1 Cui, Y., Zhong, Z. H., Wang, D. L., Wang, W. U. & Lieber, C. M. High performance silicon nanowire field effect transistors. *Nano Lett.* 3, 149-152, doi:10.1021/nl025875l (2003).
- 2 Huang, Y., Duan, X. F., Cui, Y., Lauhon, L. J., Kim, K. H., Lieber, C. M. Logic gates and computation from assembled nanowire building blocks. *Science* 294, 1313-1317, doi:10.1126/science.1066192 (2001).
- 3 Michel, J., Liu, J. & Kimerling, L. C. High-performance Ge-on-Si photodetectors. *Nat. Photonics* 4, 527-534, doi:10.1038/nphoton.2010.157 (2010).
- 4 Cui, Y., Wei, Q. Q., Park, H. K. & Lieber, C. M. Nanowire nanosensors for highly sensitive and selective detection of biological and chemical species. *Science* 293, 1289-1292, doi:10.1126/science.1062711 (2001).
- 5 Tian, B., Zheng, X., Kempa, T. J., Fang, Y., Yu, N., Yu, G., Huang, J., Lieber, C. M. Coaxial silicon nanowires as solar cells and nanoelectronic power sources. *Nature* 449, 885-U888, doi:10.1038/nature06181 (2007).

- 6 Yan, R., Gargas, D. & Yang, P. Nanowire photonics. *Nat. Photonics* 3, 569-576, doi:10.1038/nphoton.2009.184 (2009).
- 7 Yoon, J. S., Rim, T., Kim, J., Kim, K., Baek, C. K., Jeong, Y. H. Statistical variability study of random dopant fluctuation on gate-all-around inversion-mode silicon nanowire field-effect transistors. *Appl. Phys. Lett.* 106, doi:10.1063/1.4914976 (2015).
- 8 Koenraad, P. M. & Flatte, M. E. Single dopants in semiconductors. *Nat. Mater.* 10, 91-100, doi:10.1038/nmat2940 (2011).
- 9 Duffy, R., Shayesteh, M., Thomas, K., Pelucchi, E., Yu, R., Gangnaik, A., Georgiev, Y. M., Carolan, P., Petkov, N., Long, B., Holmes, J. D. Access resistance reduction in Ge nanowires and substrates based on non-destructive gas-source dopant in-diffusion. *J. Mater. Chem. C* 2, 9248-9257, doi:10.1039/c4tc02018a (2014).
- 10 Long, B., Alessio Verni, G., O'Connell, J., Holmes, J. D., Shayesteh, M., O'Connell, D., Duffy, R. Molecular layer doping: Non-destructive doping of silicon and germanium. *Proceedings of the 20th International Conference on Implantation Technology*. 1-4, doi:10.1109/iit.2014.6939995 (2014)
- 11 O'Connell, J., Verni, G. A., Gangnaik, A., Shayesteh, M., Long, B., Georgiev, Y. M., Petkov, N., McGlacken, G. P., Morris, M. A., Duffy, R., Holmes, J. D. Organo-arsenic Molecular Layers on Silicon for High-Density Doping. *ACS Appl. Mater. Interfaces* 7, 15514-15521, doi:10.1021/acsami.5b03768 (2015).
- 12 Kelly, R. A., Holmes, J. D. & Petkov, N. Visualising discrete structural transformations in germanium nanowires during ion beam irradiation and subsequent annealing. *Nanoscale* 6, 12890-12897, doi:10.1039/c4nr04513k (2014).
- 13 Zeiner, C., Lugstein, A., Buchhart, T., Pongratz, P., Connell, J. G., Lauhon, L. J., Bertagnolli, E. Atypical Self-Activation of Ga Dopant for Ge Nanowire Devices. *Nano Lett.* 11, 3108-3112, doi:10.1021/nl201105k (2011).
- 14 Yu, R., Georgiev, Y. M., Das, S., Hobbs, R. G., Povey, I. M., Petkov, N., Shayesteh, M., O'Connell, D., Holmes, J. D., Duffy, R. Junctionless nanowire transistor fabricated with high mobility Ge channel. *Phys. Status Solidi RRL* 8, 65-68, doi:10.1002/pssr.201300119 (2014).
- 15 Guilloy, K., Pauc, N., Robin, E., Calvo, V., Gentile, P., Foubert, K., Rothman, J., Reboud, V., Chelnokov, A., Benevent, V., Hartmann, J. M. Band structure engineering of strained and doped germanium nanowires and 2D layers. *IEEE Int. Conf. IV Photonics, 11th* 233-234 doi:10.1109/Group4.2014.6961940 (2014).
- 16 Priolo, F., Gregorkiewicz, T., Galli, M. & Krauss, T. F. Silicon nanostructures for photonics and photovoltaics. *Nat. Nanotechnol.* 9, 19-32, doi:10.1038/nnano.2013.271 (2014).

- 17 Duffy, R., Shayesteh, M., McCarthy, B., Blake, A., White, M., Scully, J., Yu, R., Kelleher, A. M., Schmidt, M., Petkov, N., Pelaz, L., Marques, L. A. The curious case of thin-body Ge crystallization. *Appl. Phys. Lett.* 99, doi:10.1063/1.3643160 (2011).
- 18 Duffy, R. Van Dal, M. J. H., Pawlak, B. J., Kaiser, M., Weemaes, R. G. R., Degroote, B., Kunnen, E., Altamirano, E. Solid phase epitaxy versus random nucleation and growth in sub-20nm wide fin field-effect transistors. *Appl. Phys. Lett.* 90, doi:10.1063/1.2749186 (2007).
- 19 Barth, S., Boland, J. J. & Holmes, J. D. Defect transfer from nanoparticles to nanowires. *Nano Lett.* 11, 1550-1555, doi:10.1021/nl104339w (2011).
- 20 Geaney, H., Dickinson, C., Weng, W. H., Kiely, C. J., Barrett, C. A., Gunning, R. D., Ryan, K. M. Role of Defects and growth directions in the formation of periodically twinned and kinked unseeded germanium nanowires. *Cryst. Growth Des.* 11, 3266-3272, doi:10.1021/cg200510y (2011).
- 21 Marques, L. A., Pelaz, L., Santos, I., Lopez, P. & Duffy, R. Molecular dynamics simulation of the regrowth of nanometric multigate Si devices. *J. Appl. Phys.* 111, doi:10.1063/1.3679126 (2012).
- 22 Jun, K., Joo, J. & Jacobson, J. M. Focused ion beam-assisted bending of silicon nanowires for complex three dimensional structures. *J. Vac. Sci. Technol. B* 27, 3043-3047, doi:10.1116/1.3259919 (2009).
- 23 Ronning, C., Borschel, C., Geburt, S. & Niepelt, R. Ion beam doping of semiconductor nanowires. *Mater. Sci. Eng., R* 70, 30-43, doi:10.1016/j.mser.2010.07.002 (2010).
- 24 Das Kanungo, P., Koegler, R., Zakharov, N., Werner, P., Scholz, R., Skorupa, W. Characterization of Structural Changes Associated with Doping Silicon Nanowires by Ion Implantation. *Cryst. Growth Des.* 11, 2690-2694, doi:10.1021/cg200108u (2011).
- 25 Pecora, E., Irrera, A., Boninelli, L., Spinella, C., Priolo, F. Nanoscale amorphization, bending and recrystallization in silicon nanowires. *Appl. Phys. A: Mater. Sci. Process* 102, 13-19, doi:10.1007/s00339-010-6040-2 (2011).
- 26 Fukata, N., Takiguchi, R., Ishida, S., Yokono, S., Hishita, S., Murakami, K. Recrystallization and Reactivation of Dopant Atoms in Ion-Implanted Silicon Nanowires. *ACS Nano* 6, 3278-3283, doi:10.1021/nm300189z (2012).
- 27 Zhang, Y. F., Tang, Y. H., Wang, N., Lee, C. S., Bello, I., Lee, S. T. Germanium nanowires sheathed with an oxide layer. *Phys. Rev. B: Condens. Matter Mater. Phys.* 61, 4518-4521 (2000).
- 28 Seo, K. I., Sharma, S., Yasserli, A. A., Stewart, D. R. & Kamins, T. I. Surface charge density of unpassivated and passivated metal-catalyzed silicon

- nanowires. *Electrochem. Solid-State Lett.* 9, G69-G72, doi:10.1149/1.2159295 (2006).
- 29 Grossklaus, K. A., Banerjee, A., Jahangir, S., Bhattacharya, P. & Millunchick, J. M. Misorientation defects in coalesced self-catalyzed GaN nanowires. *J. Cryst. Growth* 371, 142-147, doi:10.1016/j.jcrysgr.2013.02.019 (2013).
- 30 Romano, L., Rudawski, N. G., Holzworth, M. R., Jones, K. S., Choi, S. G., Picraux, S. T. Nanoscale manipulation of Ge nanowires by ion irradiation. *J. Appl. Phys.* 106, doi:10.1063/1.3267154 (2009).
- 31 Borschel, C., Spindler, S., Lerose, D., Bochmann, A., Christiansen, S. H., Nietzsche, S., Oertel, M., Ronning, C. Permanent bending and alignment of ZnO nanowires. *Nanotechnology* 22, doi:10.1088/0957-4484/22/18/185307 (2011).
- 32 Gomez-Selles, J. L., Darby, B. L., Jones, K. S. & Martin-Bragado, I. Lattice kinetic Monte Carlo modeling of germanium solid phase epitaxial growth. *Phys. Status Solidi C* 11, 93-96, doi:10.1002/pssc.201300159 (2014).
- 33 Darby, B. L., Yates, B. R., Martin-Bragado, I., Gomez-Selles, J. L., Elliman, R. G., Jones, K. S. Substrate orientation dependence on the solid phase epitaxial growth rate of Ge. *J. Appl. Phys.* 113, doi:10.1063/1.4776718 (2013).
- 34 Pelaz, L., Marques, L., Aboy, M., Lopez, P., Santos, I., Duffy, R. Atomistic process modeling based on Kinetic Monte Carlo and Molecular Dynamics for optimization of advanced devices. *IEEE Int. Electron Devices Meet.* 1-4, doi:10.1109/iedm.2009.5424309 (2009).
- 35 Hobbs, R. G., Schmidt, M., Bolger, C. T., Georgiev, Y. M., Fleming, P., Morris, M. A., Petkov, N., Holmes, J. D., Xiu, F. X., Wang, K. L., Djara, V., Yu, R., Colinge, J. P. Resist-substrate interface tailoring for generating high-density arrays of Ge and Bi₂Se₃ nanowires by electron beam lithography. *J. Vac. Sci. Technol., B* 30, doi:10.1116/1.4724302 (2012).
- 36 Ran, Y., Das, S., Hobbs, R., Georgiev, Y., Ferain, I., Razavi, P., Akhavan, N. D., Colinge, C. A., Colinge, J. Top-down process of germanium nanowires using EBL exposure of hydrogen silsesquioxane resist. *J. Ultimate Integr. Silicon* 145-148, doi: 10.1109/ulis.2012.6193378 (2012).
- 37 Plimpton, S. Fast parallel algorithms for short-range molecular dynamics. *J. Computat. Phys.* 117, 1-19, doi:10.1006/jcph.1995.1039 (1995).
- 38 Posselt, M. & Gabriel, A. Atomistic simulation of amorphous germanium and its solid phase epitaxial recrystallization. *Phys. Rev. B* 80, doi:10.1103/PhysRevB.80.045202 (2009).
- 39 Luedtke, W. D. & Landman, U. Preparation, structure, dynamics, and energetics of amorphous silicon: A molecular-dynamics study. *Phys. Rev. B:*

- Condens. Matter Mater. Phys.* 40, 1164-1174, doi:10.1103/PhysRevB.40.1164 (1989).
- 40 Berendsen, H. J. C., Postma, J. P. M., van Gunsteren, W. F., DiNola, A. & Haak, J. R. Molecular dynamics with coupling to an external bath. *J. Chem. Phys.* 81, 3684-3690, doi:10.1063/1.448118 (1984).
- 41 Wang, Y., Hu, Y. Z. & Irene, E. A. Electron –cyclotron-resonance plasma and thermal-oxidation mechanisms of germanium. *J. Vac. Sci. Technol., A* 12, 1309-1314, doi:10.1116/1.579313 (1994).
- 42 Bender, H., Deveirman, A., Vanlanduyt, J. & Amelinckx, S. HREM investigation of twinning in very high-dose phosphorus ion-implanted silicon. *Appl. Phys. A* 39, 83-90, doi:10.1007/bf00616823 (1986).
- 43 Su, Z., Dickinson, C., Wan, Y., Wang, Z., Wang, Y., Sha, J., Zhou, W. Crystal growth of Si nanowires and formation of longitudinal planar defects. *CrystEngComm* 12, 2793-2798, doi:10.1039/b925198g (2010).
- 44 Kelly, P. M., Wauchope, C. J. & Zhang, X. Calculation of overall tilt angles for a double tilt holder in a TEM. *Microsc. Res. Tech.* 28, 448-451, doi:10.1002/jemt.1070280512 (1994).
- 45 Csepregi, L., Küllen, R. P., Mayer, J. W. & Sigmon, T. W. Regrowth kinetics of amorphous Ge layers created by ⁷⁴Ge and ²⁸Si implantation of Ge crystals. *Solid State Commun.* 21, 1019-1021, doi:10.1016/0038-1098(77)90009-6 (1977).
- 46 Priolo, F., Battaglia, A., Nicotra, R. & Rimini, E. Low-temperature reordering in partially amorphized Si crystals. *Appl. Phys. Lett.* 57, 768-770, doi:10.1063/1.103415 (1990).
- 47 Johnson, B. C., Gortmaker, P. & McCallum, J. C. Intrinsic and dopant-enhanced solid-phase epitaxy in amorphous germanium. *Phys. Rev. B* 77, 214109 doi:10.1103/PhysRevB.77.214109 (2008).
- 48 Borschel, C. & Ronning, C. Ion beam irradiation of nanostructures - A 3D Monte Carlo simulation code. *Nucl. Instrum. & Methods Phys. Res. B* 269, 2133-2138, doi:10.1016/j.nimb.2011.07.004 (2011).
- 49 den Hertog, M. I., Cayron, C., Gentile, P., Dhalluin, F., Oehler, F., Baron, T., Rouviere, J. L. Hidden defects in silicon nanowires. *Nanotechnology* 23, doi:10.1088/0957-4484/23/2/025701 (2012).
- 50 Drosd, R. & Washburn, J. Some observations on the amorphous to crystalline transformation in silicon. *J. Appl. Phys.* 53, 397-403, doi:10.1063/1.329901 (1982).
- 51 Olson, G. L. & Roth, J. A. Kinetics of solid phase crystallization in amorphous silicon. *Mater. Sci. Rep.* 3, 1-77, doi:10.1016/S0920-2307(88)80005-7 (1988).
- 52 Donovan, E. P., Spaepen, F., Turnbull, D., Poate, J. M. & Jacobson, D. C. Calorimetric studies of crystallization and relaxation of amorphous Si and Ge

- prepared by ion implantation. *J. Appl. Phys.* 57, 1795-1804, doi:10.1063/1.334406 (1985).
- 53 Lu, G. Q., Nygren, E. & Aziz, M. J. Pressure-enhanced crystallization kinetics of amorphous Si and Ge: Implications for point-defect mechanisms. *J. Appl. Phys.* 70, 5323-5345, doi:10.1063/1.350243 (1991).
- 54 Haynes, T. E., Antonell, M. J., Lee, C. A. & Jones, K. S. Composition dependence of solid-phase epitaxy in silicon-germanium alloys: Experiment and theory. *Phys. Rev. B: Condens. Matter Mater. Phys.* 51, 7762-7771 doi:10.1103/PhysRevB.51.7762 (1995).
- 55 Kringhøj, P. & Elliman, R. G. Solid-Phase Epitaxial Crystallization of Strain-Relaxed $\text{Si}_{1-x}\text{Ge}_x$ Alloy Layers. *Phys. Rev. Lett.* 73, 858-861 doi:10.1103/PhysRevLett.73.858 (1994).
- 56 Li, D., Nielsen, M. H., Lee, J. R. I., Frandsen, C., Banfield, J. F., De Yoreo, J. J. Direction-Specific Interactions Control Crystal Growth by Oriented Attachment. *Science* 336, 1014-1018, doi:10.1126/science.1219643 (2012).
- 57 Mecklenburg, M., Hubbard, W. A., White, E. R., Dhall, R., Cronin, S. B., Aloni, S., Regan, B. C. Nanoscale temperature mapping in operating microelectronic devices. *Science* 347, 629-632, doi:10.1126/science.aaa2433 (2015).
- 58 Hobbs, R. G., Petkov, N. & Holmes, J. D. Semiconductor Nanowire Fabrication by Bottom-Up and Top-Down Paradigms. *Chem. Mater.* 24, 1975-1991, doi:10.1021/cm300570n (2012).
- 59 Posselt, M., Bischoff, L., Grambole, D. & Herrmann, F. Competition between damage buildup and dynamic annealing in ion implantation into Ge. *Appl. Phys. Lett.* 89, doi:10.1063/1.2360238 (2006).

4.7. Appendix

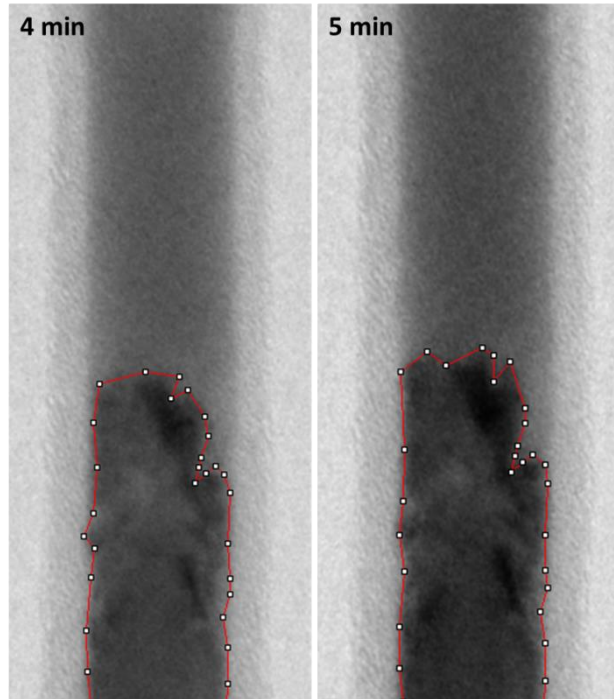


Figure 4.A. Area of crystal region measured from in-situ anneal images for NW1.

The method used to calculate the rates of crystallization presented in this study:

The grown nanowire is assumed to have a circular cross section, i.e. a cylindrical shape nanowire. The cross sectional area of the nanowire is calculated $=\pi r^2$. This area was taken and the volume was averaged to assume a square cross section, i.e. cuboid shape nanowire, and the square root of the circular cross section was determined as the effective depth of the nanowire. When an amorphous area was measured (as shown in Figure 4.A), this was multiplied by the effective depth to calculate an approximate volume in nm^3 . To convert the volume into number of atoms (to make the units relatable to the simulation data) this volume was multiplied by the number of atoms per nm^3 which for Ge is $44.355 \text{ atoms nm}^{-3}$.

Chapter 4. Epitaxial post-implant recrystallization in germanium nanowires

Molecular dynamics simulations were contributed by Dr Bartosz Liedke, Dr Matthias Posselt and Mr Stefan Baldauf of Helmholtz Zentrum Dresden Rossendorf, Institute of Ion Beam Physics and Materials Research in Dresden. In this study the LAMMPS program was employed³⁷ with a Stillinger-Weber-type interatomic potential.³⁸ The simulation cell used for the calculation were cuboids with a size of $20 \times 20 \times 30 a^3$ and $20 \times 20 \times 60 a^3$, i.e. initially with a total of 96000 and 192000 atoms, respectively, where $a = 5.657 \text{ \AA}$ is the lattice parameter of c-Ge. Simulation cells with long sides parallel to the $\langle 111 \rangle$ and the $\langle 100 \rangle$ crystal axes were considered in order to study NWs with these orientations. Periodic boundary conditions in three directions and a canonical ensemble (NVT) were used. The amorphous region was prepared by the method of Luedtke et al.³⁹ via slow cooling from the melt at a rate of 1 K ps^{-1} , analogically to the work of Posselt et al.³⁸ To obtain a NW with free surfaces in x- and y-directions, all atoms within the distance of $5a$ from the x,y-borders of the simulation cell were removed. The resulting systems with 24000 (for $20 \times 20 \times 30a^3$ simulation cell) and 48000 atoms (for $20 \times 20 \times 60a^3$ simulation cell) consist of two c/a interfaces as shown in Figure 4.B (a) and (c). In recrystallization calculations at 700, 750, 800, and 900 K (426.85, 476.85, 526.85, and 626.85 °C, respectively) a Berendsen thermostat was used.⁴⁰ Zero pressure (stress) was maintained at the cell boundaries in both z-directions using a Berendsen barostat.

Molecular dynamics (MD) calculations are presented (by Dr Bartosz Liedke, Dr Matthias Posselt and Mr Stefan Baldauf of Helmholtz Zentrum Dresden Rossendorf, Institute of Ion Beam Physics and Materials Research in Dresden) in Figure 4.B for a

$\langle 111 \rangle$ grown NW. The notable comparison between the MD calculations and the experimental results is the trend of an initial linear growth followed by a saturation of the recrystallization rate (regions B and C in Figure 4.6 g and in Figure 4.7 g). From the MD calculations in figure 4.B (a), it can be observed that the initial average growth rate is approximately 1×10^{12} atoms s^{-1} for the first 6 ns. The observed average rate for the time from 6 to 16 ns is approximately 6×10^{11} atoms s^{-1} which is a drop to 60% of the initial average rate. The absolute values of simulated recrystallization rates are larger than the measured data. This is related to the quality of the interatomic potential used in the calculations, which was designed to reproduce realistic properties of crystalline, amorphous and liquid Ge but does not describe SPEG quantitatively correct. Therefore the comparison with experimental results is focused on the general trends regarding the recrystallization process and not on the absolute values of the recrystallization rates.

MD calculations have also been presented for a $\langle 100 \rangle$ grown nanowire in Figure 4.B (c) and (d). Three different rates of SPEG are visible for each curve, except 700 K annealing, where saturation has not yet been achieved. Decrease of the regrowth rate in the first few ns of annealing for each temperature suggests a considerable importance of confinement effects. The rates decrease again after the two fronts of recrystallization meet in the middle of the supercell. The thick lines are the linear fits applied for the initial slopes, used to calculate activation energy of SPEG that equals 0.92 eV.

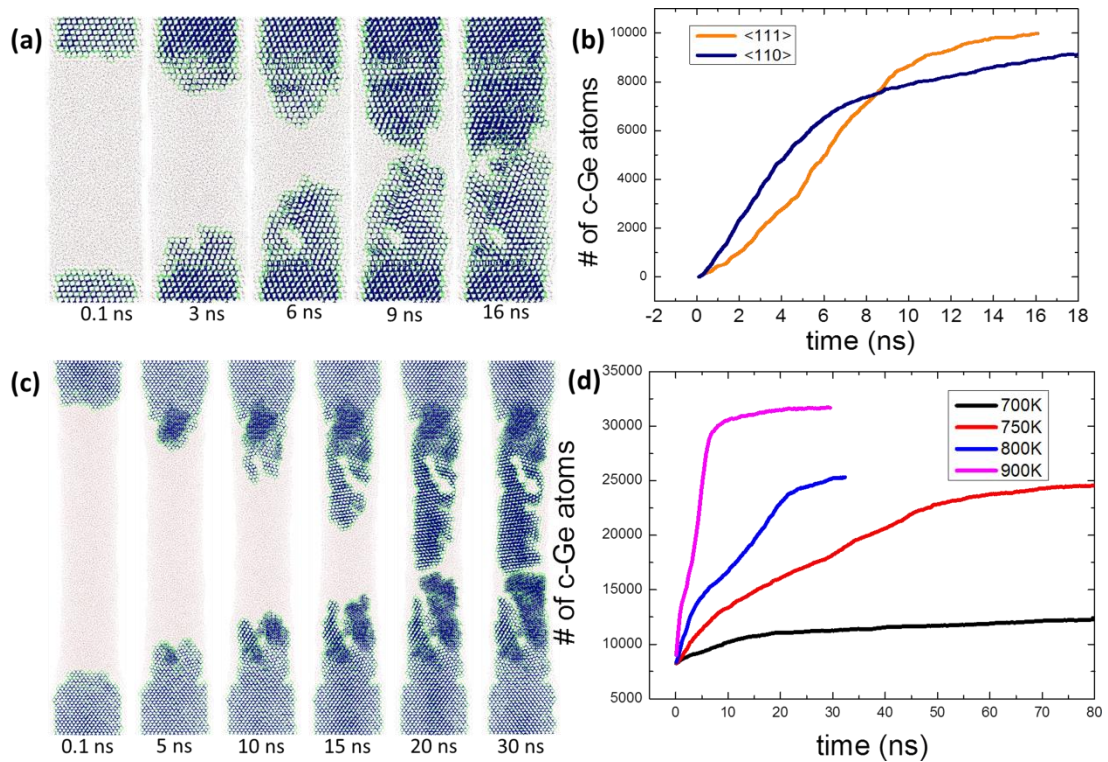


Figure 4.B. These calculations were contributed to the work by Dr Bartosz Liedke, Dr Matthias Posselt and Mr Stefan Baldauf of Helmholtz Zentrum Dresden Rossendorf, Institute of Ion Beam Physics and Materials Research in Dresden. (a) Molecular dynamics simulation of recrystallization of a $\langle 111 \rangle$ grown Ge NWs at 800K. (b) Comparison of SPEG of NWs for two orientations $\langle 100 \rangle$ and $\langle 111 \rangle$ shows a very similar growth rate using MD calculations. Simulation cell size is $20 \times 20 \times 30a^3$, where $a = 5.657 \text{ \AA}$ in both figures (a) and (b). (c) $\langle 100 \rangle$ growth in Ge NW at $T=800\text{K}$ (d) $\langle 100 \rangle$ growth in Ge NWs at varied T : 700K, 750K, 800K and 900K. Simulation cell size is $20 \times 20 \times 60a^3$, where $a = 5.657 \text{ \AA}$ in both figures (c) and (d).



Kelly, R.A 2016. Modifying germanium nanowires for future devices: an in situ TEM study. PhD Thesis, University College Cork.

Please note that Chapter 5 (pp.113-142) is unavailable due to a restriction requested by the author.

CORA Cork Open Research Archive <http://cora.ucc.ie>

Chapter 6

Conclusions and Outlook

Chapter 6. Conclusions and Outlook

A disturbance in the trend of Moore's law is becoming ever more inevitable as issues arise with Si processing.¹ The advantage of the stable SiO₂ is becoming obsolete due to gate leakage, opening the way for materials with better intrinsic electrical mobilities such as Ge, which had been previously overlooked due to issues with an unstable oxide.² If semiconductor NWs are to be incorporated into future electronic devices we need to fully understand, at the nanoscale, the implications of altering the structures to achieve the desired electrical properties.³ The aim of this thesis was to explore some of the fundamental issues of Ge NW incorporation into future semiconductor devices. Typical fab processes have been applied, i.e. ion beam doping, crystal recovery post ion beam irradiation and germanide formation, to investigate the mechanism of the process and its effect on the NW.

Chapter 1 introduced the role of dynamic TEM for fundamental understanding of semiconductor nanostructures for future nanoelectronic devices. In situ TEM provides stepping stones to understand the fundamental properties of semiconductor nanowires. No stand-alone technique can provide all the answers but dynamic TEM can provide large pieces to the puzzle. With state of the art double aberration corrected TEMs with monochromators and equipped with analytical tools such as EELS and EDX coupled with in situ TEM holders, dynamic processes can be studied with potentially atomic resolution, particularly for 1-dimensional materials such as graphene.⁴ This is a fascinating and broad area of research as shown by the diverse properties investigated in semiconductor nanowires discussed in the chapter.

Chapter 2 focused on the damage incurred in Ge NWs post ion irradiation. Nanowires suspended on FIB-labelled SiN membranes were irradiated in a stepwise

Chapter 6. Conclusions and Outlook

manner to monitor the damage build up with increasing ion flux. The results provided an understanding of the mechanism of the damage build up in NWs. A dependence on the shape and diameter of a NW and the ion energy used was established. It would be of interest to conduct these experiments under cryogenic and elevated temperature conditions. An increase in the damage is expected at the cryogenic temperatures as dynamic annealing would be eliminated at such low temperatures. The elevated temperatures would promote dynamic annealing however. As instruments are becoming more advanced and integrated, the potential to observe a single ion cascade event within a nanostructure at lattice or atomic resolution is becoming realistically achievable.⁵ Operating conditions of the electron beam would need to be considered as the beam could introduce energy which would promote dynamic annealing and produce false results. Nanostructures are ideal as they do not require any sample preparation techniques prior to TEM/irradiation and hence the samples are “pure” prior to irradiation.

Chapter 3 extended on methods and results described in chapter 2, with a focus on the thermal recovery of the crystal structure post ion irradiation. The main message to take from this chapter is that not only is a crystal seed required but also the external stresses on a NW determine the quality of the recovered crystallinity, i.e. polycrystalline or single crystalline and with the evolution of defects or not. Recrystallization within a NW is complex due to many competing factors including the competition between RNG and SPEG. SPEG is promoted when a crystal seed remains whereas RNG is promoted when the NW experiences strain. The high surface-area to volume ratio also increases the sensitivity of NWs to surface

Chapter 6. Conclusions and Outlook

roughness and stacking fault formation at the surface has been observed. To study structures produced via the top-down lithography approach; NWs could be defined on GeOI followed by a back etch through the bulk Si. The buried oxide would act as an etch stop and open a window for TEM imaging. This approach would provide NWs on a stable support which would facilitate ion irradiation followed by observation within the TEM without the need to extract the structures in a FIB cross section. The oxide would need to be thin enough to be electron transparent but thick enough to be a stable support for the Ge NWs, for example 100 nm.

Chapter 4 detailed an experimental set up for in situ observation of Ni-germanide formation in Ge nanopillars. The method facilitates a range of Ge nanostructures with the same crystal orientation, here all substrates used were (001). An angled growth front was observed showing that germanide growth along the (001) orientation is not favourable.⁶ Size dependence was observed for the temperature at which the Ni migration occurs at lower temperatures for smaller diameter structures. The variation in germanide formation from pillar to pillar and even within a pillar is attributed to the polycrystalline nature of the Ni seed. To investigate further the effect of the crystallinity of the Ni seed it is proposed that a single crystalline Ni seed should be used. One possible route would entail single crystalline (and ideally defect-free) Ni nanoparticles as the seed/etch mask for the nanopillar. One difficulty would be achieving a monolayer or sparsely dispersed Ni nanoparticles on a Ge substrate to achieve the individual nanopillars with clean etched sidewalls.^{7,8}

Chapter 6. Conclusions and Outlook

Certain materials and/or mechanisms may be sensitive to the beam energy during in situ TEM experiments. These materials/mechanisms require ultrafast TEM techniques which allow fast acquisition and do not rely on a long exposure to achieve a high resolution image. Taking into account the effect the beam energy on a sample is vital as has been shown for Si nanostructures at high beam energies by Vanhellefont et al. (2MeV) and Fedina et al. (400keV).^{8,9} To achieve high resolution images it should be a simple case of increasing the energy of the electron beam (in the MeV range) to decrease the wavelength of the electrons and in turn increase the spatial resolution. In the ideal world this should increase linearly, however, it was found that the wavelength of the electrons was not the only factor that limited the resolution of the TEM. In fact, aberrations in the lens, namely spherical (C_s) and chromatic (C_c) prevent ideal spatial resolution capabilities.¹⁰ In modern commercial state-of-the-art (S)TEMs, the instrument operates within the low (<200 keV) and/or intermediate (200-400 keV) energy range and is equipped with double aberration correction and monochromators.¹¹ Single atom resolution has been demonstrated at beam energies as low as 60 keV.^{12,13} With capabilities to achieve single atom resolution at such low energies opens the potential for dynamic TEM of beam sensitive materials/mechanisms.

The future of dynamic TEM is fast approaching with state-of-the-art TEMs capable of atomic resolution (for the one-dimensional materials such as graphene), ultrafast TEM capable of ns time resolution and stabilized in situ stage holders. The range of possible dynamic TEM experiments is phenomenal as more than one stimulus can be applied to a sample. A sample can be immersed in a condition similar to its actual

Chapter 6. Conclusions and Outlook

working conditions so as to observe a truer representation of processes and mechanisms. We have so far only observed the tip of the iceberg of the capabilities of dynamic TEM.

References

- 1 Kuhn, K. J. Moore's crystal ball: Device physics and technology past the 15 nm generation. *Microelectron. Eng.* 88, 1044-1049, doi:10.1016/j.mee.2011.03.163 (2011).
- 2 Brunco, D. P., De Jaeger, B., Eneman, G., Mitard, J., Hellings, G., Satta, A., Terzieva, V., Souriau, L., Leys, F. E., Pourtois, G., Houssa, M., Winderickx, G., Vrancken, E., Sioncke, S., Opsomer, K., Nicholas, G., Caymax, M., Stesmans, A., Van Steenberghe, J., Mertens, P. W., Meuris, M., Heyns, M. M. Germanium MOSFET devices: Advances in materials understanding, process development, and electrical performance. *J. Electrochem. Soc.* 155, H552-H561, doi:10.1149/1.2919115 (2008).
- 3 Lu, W., Xie, P. & Lieber, C. M. Nanowire Transistor Performance Limits and Applications. *IEEE Trans. Electron Dev.* 55, 2859-2876, doi:10.1109/ted.2008.2005158 (2008).
- 4 Pan, C. T., Hinks, J. A., Ramasse, Q. M., Greaves, G., Bangert, U., Donnelly, S. E., Haigh, S. J. In-situ observation and atomic resolution imaging of the ion irradiation induced amorphisation of graphene. *Sci. Rep.* 4, 6334, doi:10.1038/srep06334 (2014).
- 5 Hattar, K., Bufford, D. C. & Buller, D. L. Concurrent in situ ion irradiation transmission electron microscope. *Nucl. Instrum. Methods Phys Res., Sect. B* 338, 56-65, doi:10.1016/j.nimb.2014.08.002 (2014).
- 6 Tang, J. S., Wang, C. Y., Xiu, F. X., Zhou, Y., Chen, L. J., Wang, K. L. Formation and Device Application of Ge Nanowire Heterostructures via Rapid Thermal Annealing. *Adv. Mater. Sci. Eng.* doi:10.1155/2011/316513 (2011).
- 7 Hogg, C. R., Picard, Y. N., Narasimhan, A., Bain, J. A. & Majetich, S. A. Pattern transfer with stabilized nanoparticle etch masks. *Nanotechnology* 24, doi:10.1088/0957-4484/24/8/085303 (2013).
- 8 Singh, J., Kaurav, N., Lalla, N. P. & Okram, G. S. Naturally self-assembled nickel nanolattice. *J. Mater. Chem. C* 2, 8918-8924, doi:10.1039/c4tc01360c (2014).

Chapter 6. Conclusions and Outlook

9. Vanhellefont, J., Anada, S., Nagase, T., Yasuda, H., Bender, H., Rooyackers, R., Vandooren, A. In situ UHVEM irradiation study of intrinsic point defect behavior in Si nanowire structures. *Phys. Stat. Solidi C*, doi:10.1002/pssc.201400100 (2015).
10. Fedina, L. I., Song, S. A., Chuvilin, A. L., Gutakovskii, A. K. & Latyshev, A. V. The mechanism of {113} defect formation in silicon: clustering of interstitial-vacancy pairs studied by in situ high-resolution electron microscope irradiation. *Microsc. Microanal.* 19, 38-42, doi:10.1017/s1431927613012294 (2013).
11. Mukai, M., Okunishi, E., Ashino, M., Omoto, K., Fukuda, T., Ikeda, A., Somehara, K., Kaneyama, T., Saitoh, T., Hirayama, T., Ikuhara, Y. Monochromator for aberration-corrected STEM. *Microscopy and Microanalysis* **20**, 606-607, doi: 10.1017/S1431927614004759 (2014).
12. Krivanek, O. L., Dellby, N., Murfitt, M. F., Chisholm, M. F., Pennycook, T. J., Suenaga, K., Nicolosi, V. Gentle STEM: ADF imaging and EELS at low primary energies. *Ultramicroscopy* **110**, 935-945, doi:10.1016/j.ultramic.2010.02.007 (2010).
13. Krivanek, O. L., Chisholm, M. F., Nicolosi, V., Pennycook, T. J., Corbin, G. J., Dellby, N., Murfitt, M. F., Own, C. S., Szilagy, Z. S., Oxley, M., P., Pantelides, S. T., Pennycook, S. J. Atom-by-atom structural and chemical analysis by annular dark-field electron microscopy. *Nature* **464**, 571-574, doi:10.1038/nature08879 (2010).